Title

Visualization of Porous Composite Battery Electrode Fabrication Dynamics for Different Formulations and Conditions Using Hard X–ray Microradiography

Journal

ACS Applied Energy Materials, 7(7)

ISSN

2574-0962

Authors

Higa, Kenneth

Zhang, Buyi

Chandrasiri, Dilni Kaveendi

et al.

Publication Date

2024-04-08

DOI

10.1021/acsaem.4c00402

Peer reviewed

ACS APPLIED ENERGY MATERIALS

www.acsaem.org
Article

Visualization of Porous Composite Battery Electrode Fabrication Dynamics for Different Formulations and Conditions Using Hard X-ray Microradiography

Kenneth Higa,* Buyi Zhang, Dilni Kaveendi Chandrasiri,‖ Denny Tan,‖ Daniel Collins-Wildman, Patricius Bloemhard, Eric Lizotte, Gabriela Martin-Nyenhuis, Dilworth Y. Parkinson, Ravi Prasher,‖ and Vincent S. Battaglia‖

Cite This: ACS Appl. Energy Mater. 2024, 7, 2989−3008

ABSTRACT: Porous composite battery electrode performance is influenced by a large number of manufacturing decisions. While it is common to evaluate only finished electrodes when making process adjustments, one must then make inferences about the fabrication process dynamics from static results, which makes process optimization very costly and time-consuming. To get information about the dynamics of the manufacturing processes of these composites, we have built a miniature coating and drying apparatus capable of fabricating lab-scale electrode laminates while operating within an X-ray beamline hutch. Using this tool, we have collected the first radiography image sequences of lab-scale battery electrode coatings in profile, taken throughout drying processes conducted under industrially relevant conditions. To assist with interpretation of these image sequences, we developed an automated image analysis program. Here, we discuss our observations of battery electrode slurry samples, including stratification and long-term fluid flow, and their relevance to composite electrode manufacturing.

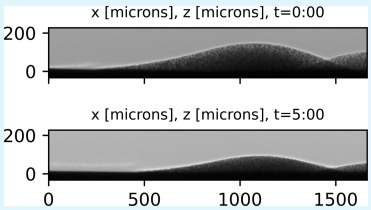

KEYWORDS: *composite electrode, lithium-ion, slurry processing, coating, casting, drying, consolidation, radiography*

1. INTRODUCTION

As in many manufacturing processes, lithium-ion battery porous composite electrode manufacturing involves a large number of decisions that influence performance of the manufactured products.[1] For instance, when mixing components into an electrode mixture, one must choose the mixing equipment, the components to be mixed, the times at which components are added to the mixture, and the operating parameters of the mixing equipment, among other variables. Applying and drying the mixture as a coating on a current collector involves, among other things, choosing the coating and drying equipment and deciding on equipment operation parameters. Complicating these scenarios are factors such as operator consistency, environmental conditions, and variability in the component materials. Despite the best of efforts, many variables will be left uncontrolled, although manufacturers can focus on controlling variables that are more influential than others.

Product samples are typically tested against quality control criteria. One might imagine that the performance score against a particular criterion is predicted by a function of the many variables representing process decisions. If one could quickly evaluate these functions, process optimization might be done very efficiently. However, being able to estimate these function values over anything but limited ranges for a reduced set of variables is impractical for many manufacturing processes. Furthermore, such an approach might not clearly indicate why particular final outcomes are observed. More complete knowledge might require observations of process dynamics.

The present work focuses on one aspect of electrode production—the drying and consolidation processes of coatings. Some recent experimental investigations of these processes are discussed in a recent review;[2] most of these, along with other recent works,[3−6] involve static observations of the final dried coatings, from which authors make inferences about the drying processes.

Previously, some of the present authors used hard X-ray microradiography and microtomography imaging to perform dynamic observations of drying drops of relatively dilute particle suspensions.[7] Hard X-ray radiography was a valuable tool for these investigations because of the ability of hard X-rays to penetrate materials that are opaque to visible light. Additionally, the short image acquisition times at X-ray light source facilities such as the Advanced Light Source permit reasonable time resolution of dynamic processes. The mixture drops were manually deposited on a stage that could be heated by conduction. Subsequent image processing showed dynamic

Received: February 16, 2024
Revised: March 8, 2024
Accepted: March 11, 2024
Published: March 25, 2024

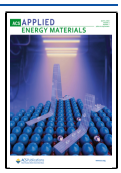

https://doi.org/10.1021/acsaem.4c00402
ACS Appl. Energy Mater. 2024, 7, 2989−3008

development of nonuniform spatial concentration distributions within the drops. Subsequently, Zenyuk and co-workers[8] used X-ray radiography to capture drying processes of larger drops consisting of inks mimicking those used to fabricate fuel cell electrodes. More recently, Xiao and co-workers[9] performed dynamic observations of small volumes of battery electrode dispersions by X-ray tomography. Small sample volumes were used in all of these studies, in contrast with the decimeter-scale coatings produced by manufacturing lines; for instance, in our earlier work,[7] the small drops with highly curved surfaces were thought to limit real-world relevance of these experiments to the edges of electrode coatings. Furthermore, the sample heating arrangements used in these studies cannot be easily translated to heating processes used industrially; for instance, in our earlier work,[7] the conductive heating of the substrate was not thought to be easily translated to industrial electrode manufacturing, which generally involves controlled infrared (IR) and/or convective heating from heat sources located above the coatings.

Unfortunately, industrially relevant observations of dynamic processes with X-ray beamlines, or even conditions that are faithful to lab-scale electrode fabrication procedures, tend to be difficult to achieve because the experimental setups are locked in beamline hutches during observation, preventing researchers from having direct access to the setups during experiments. To address this challenge, we have designed and built a novel experimental setup that allows for remotely controlled fabrication and dynamic observation of mixture-based coatings under tightly controlled, industrially relevant drying conditions. Coatings are cast using a doctor blade, as is typical in lab-scale electrode fabrication.

Here, we describe hard X-ray microradiography observations of drying electrode coatings that we have performed with this novel experimental setup. We considered variables such as mixture composition and infrared heating power that correspond to a small set of decisions taken in an electrode manufacturing process, and we have attempted to connect these decisions to dynamic drying behavior. We discuss observations such as fluid flow on long time scales and heat-driven stratification, and we reflect on implications for electrode fabrication at the laboratory scale.

2. EXPERIMENTAL SECTION

To enable reproducible X-ray microradiography observations of drying electrode coatings, we required an experimental setup that would fit into a beamline hutch while also allowing coating and heating actions to be performed under remote control. We designed and constructed a fully custom robot that uses a doctor blade to cast a manually deposited sample into a coating and places the coating into the field-of-view of the X-ray microradiography beamline. It is not reasonable to describe the details of implementation here, but fundamentally, the robot has a moving aluminum sample platform (and a manual tilt-adjustment mechanism) that drives a manually deposited mixture sample under a custom-made doctor blade and into the beam path. We positioned the assembly so that the X-ray beam path, determining the observation position, was situated underneath an infrared (IR) quartz heating lamp (Ceramicx SQE-150/120) with an open face of approximately 4 in. by 4.75 in., controlled to a time-averaged power level using pulse-width modulation. The heating element has a listed "useful wavelength range" of 1.5−8 μm and was mounted to put the face of the lamp approximately 2 cm above the sample platform, with the beam path located below the approximate horizontal center of the heating element. Remote control was achieved through instructions sent over a USB cable routed into the beamline hutch to a BeagleBone Black single-board computer running our custom controller software system, which will be considered for release as open-source software pending further development.

Radiography experiments were conducted at the Advanced Light Source (ALS) beamline 8.3.2 (hard X-ray microtomography/microradiography), with photon energy set to 23 keV. X-rays passed through samples reach a LuAG:Ce scintillator, which emits visible light that passes through a 10× lens and is detected by a PCO Edge camera. Each pixel edge in the resulting images corresponds to a distance of approximately 0.639 μm.

During the initial setup of the apparatus in the beamline 8.3.2 hutch, a precision digital leveler was used to set the heights of the adjustable feet of the robot for coarse alignment of the sample platform with the motorized tomography stage of the beamline hutch, used here only for reference. Then prior to each experiment, the manual tilt-adjustment mechanism was used to bring the platform into alignment with the X-ray beam to prevent platform tilting from obscuring coatings that are only tens of microns in height.

Polyacrylic acid (PAA) binder (450,000 g/mol) solution was prepared by adding PAA powder at 10% by weight into deionized (DI) water and leaving the mixture overnight on a roller mill operating at 20 rotations per minute (rpm). Following previous work,[10] we also prepared lithium-substituted PAA (Li-PAA) solution as follows. First, a 14% (by mass) aqueous PAA solution was prepared overnight on a roller mill operating at 20 rpm. Then a 1 molar aqueous LiOH solution was added dropwise to the 14% PAA solution with a magnetic stir bar operating at 250 rpm until the pH of the solution was greater than 4. Additional water was added to adjust the concentration of PAA to 10% by mass. The final pH of the Li-PAA solution was around 4.5. A similar protocol was used to prepare the 10% cesium-substituted PAA (Cs-PAA) solution, and its final pH was maintained close to 4.5. Other researchers have made these substitutions for hydrogen atoms to improve electrochemical performance in the case of lithium[11,12] and to make the binder easier to detect in the case of cesium,[13] which is much less transmissive than hydrogen to X-rays.

Sets of four identical mixture samples were prepared with silica/acetylene black (AB)/binder mass ratios of 8:1:1, as follows. Silica [MSE Supplies] with a volume-weighted average particle diameter (commonly labeled as "D-50") of 7 μm (as determined by a Malvern Mastersizer 3000 instrument) and AB were dry-mixed in 24 mL Yamayu 3−53 containers with a planetary centrifugal ball mill [MSE supplies mini planetary mill] at 600 rpm, in two 3 min intervals with 1 min of rest to allow the material to cool. 5 mm yttria-stabilized zirconia beads were used as milling balls, with a powder-to-bead weight ratio of 1:5. Next, PAA solution, Li-PAA solution,[11,12] or Cs-PAA binder solution was added to each container of dry-mixed powder, along with additional solvent consisting of 1% by weight of isopropyl alcohol (IPA) in DI water. The containers were returned to the planetary centrifugal ball mill for additional mixing at 600 rpm for 4 intervals of 3 min; mixtures of "low," "medium," and "high" concentrations were prepared with liquid weight percentages of 76.6, 70, and 63, respectively, which is consistent with others' formulations.[10,14] Each sample container was then transferred to a rolling mill operating at 20 rpm and left for approximately 12 h before being brought to the beamline just prior to observation. For each sample, the delay between retrieval from the rolling mill and the start of the experiment was typically shorter than half an hour.

Three "low AB" mixture samples were prepared with lithium nickel manganese cobalt oxide (NMC 622)/AB/polyvinylidene difluoride (PVDF) mass ratios of 9.8:0.088:0.112, with 10:2.5 ("high"), 10:4 ("medium"), and 10:5.5 ("low") ratios of NMC 622 to *N*-methyl-2-pyrrolidone (NMP). Three "high AB" mixture samples were prepared with NMC 622/AB/PVDF mass ratios of 9.28:0.32:0.4, in 10:5 ("high" concentration), 10:7 ("medium"), and 10:9.5 ("low") ratios of NMC 622 to NMP. NMC (supplied by Umicore with D-50 size provided as 11.8 μm) was dry-mixed with AB by hand. The appropriate amount of NMP was added, and a rotor-stator homogenizer operating at 5000 rpm was used to mix for 25 min. A solution of 10% PVDF (by weight) in NMP was then added to the mixture, and mixing continued for 1 h at 3000 rpm. The temperature of the slurry was checked with an IR

https://doi.org/10.1021/acsaem.4c00402
ACS Appl. Energy Mater. 2024, 7, 2989−3008

thermometer to ensure that the temperature of the slurry did not rise above 38 °C.

Battery-grade copper foil substrates were carefully cut to avoid deformation. For each experiment, one such substrate was smoothed onto the sample platform and held in place with a thin layer of water. As this substrate placement process placed some mechanical stress on the platform, platform tilt alignment was performed prior to almost every experiment.

Four experiments at a range of heating powers were performed with each set of four identical mixture samples. Following platform alignment, a mixture sample was manually deposited with by pipet on the foil substrate, and the beamline hutch doors were immediately closed. Radiography images at regular intervals (typically with 300 ms exposure and 4.7 s delay between exposures) were collected through the end of each experiment. After starting image collection and obtaining at least one "background" image, control signals were sent to the apparatus to drive the sample platform under the doctor blade (with blade height fixed at 400 μm above the substrate surface), then to lift the doctor blade safely off of the platform, and finally to put the coating into the beam path for observation and activate the IR heater mounted above the beam path. The platform was driven at a speed of approximately 4.2 cm/s. This process was automated, putting the sample platform in place for observation within 15 s of completion of the coating process, with the beam path roughly aligned with the horizontal center of the coating (along the direction of platform motion). The start of image collection was not precisely timed with the coating and drying operations because these were controlled by different computers. For simplicity, we have defined time $t = 0$ to correspond to the first clear image showing the sample platform in each experiment (that is, not taken during platform movement). Following each experiment, the laminates were carefully peeled from the platform and stored.

Although it was impractical for us to fully return the entire apparatus to room temperature between each experiment, each experiment was separated in time by at least 15 min due to the need for cleaning and alignment.

2.1. Image Processing. The radiography experiments outlined above produce sequences of raw transmission images, resulting from interaction of the X-ray beam with the full thickness of the part of the sample coating through which it passes. These grayscale images have 16 bit integer values $I_r(x, z)$ assigned to each pixel position (x, z) in the camera field-of-view. Higher values correspond to higher intensities of visible light emitted by the scintillator and detected by the camera, corresponding to higher intensities of incoming X-ray light, with all relationships being linear. Higher intensities of incoming X-rays reaching the scintillator ideally correspond to higher X-ray transmission through parts of the sample (X-ray photons are more likely to interact with material containing more electrons, whether due to density or atomic composition), but sometimes also resulting from X-ray refraction by parts of the sample, as at interfaces.

These images are processed with a custom Python program, which first removes image distortions that are unrelated to the samples. Images collected just prior to positioning of the sample platform in the beam path can be interpreted as bright-field background images with pixel values $I_b(x, z)$. These can be imagined as showing transmission through a distorting layer that is always present. The intensity of light emerging through this "distorting layer" should then be considered when examining all other transmission images in order to isolate the transmission through the sample. The pixel values in the raw images are therefore corrected by dividing by the values of pixels in the corresponding positions in a bright-field image, producing images with floating-point pixel values $T(x, z) = I_r(x, z)/I_b(x, z)$, which we will call "transmission fraction" and which ideally would always be less than 1, but which in reality can be greater than 1 due to noise and phase contrast artifacts. To reduce storage space and processing time, these were converted to 16 bit unsigned integer values. We determined that storing pixel values obtained by rounding $2^{14}T(x, z) = 16384T(x, z)$ avoided integer overflows in any of the image sequences. In the coating profile images that will be shown later, we have imposed a pixel value ceiling of 2 when needed, which improves contrast and which causes negligible distortion, resetting the values of at most a few noisy pixels with large values. In other cases, we also employ averages over larger numbers of pixels, which eliminates the need for an imposed pixel value ceiling.

Small errors in platform leveling, platform and substrate thickness, and camera angle are possible, which can lead to the substrate surface not occupying a perfect horizontal line of pixels in the radiography images. Recognizing this, we perform substrate surface detection in our image processing program. Visual inspection of the image sequences suggested that air, coating, and substrate/platform regions are often clearly distinguishable and might be automatically distinguished by applying a threshold segmentation procedure. As with many image processing techniques, use of a particular threshold value introduces subjectivity, as does the very choice to apply threshold segmentation.

The ImageJ[15] program was used manually to determine these threshold pixel values (corresponding to transmission fractions of 0.031 and 0.22) that, based on visual inspection, consistently distinguish among air, coating, and substrate/platform regions throughout all image sequences. Our custom Python program uses the OpenCV[16] library to automatically apply these thresholds and then assembles a list for which the discrete Laplacian is nonzero. As a simple noise-removal heuristic, only the pixel closest to the bottom (top) of the image in each column is retained when seeking the coating/substrate (air/coating) interface. Linear least-squares fits of straight lines to the remaining pixel positions using the NumPy[17] library are then used to determine lines that describe these interfaces. As discussed below, these can change in position over time, so vertical positions are reported relative to the substrate height. Specifically, for each image, we reference heights to the end of the coating/substrate line that is closest to the bottom of the image.

Finally, to survey image data from all images in a sequence, we construct what we will call "condensed time-progression" images to examine these variations. For such an image, the left column of pixels has values determined by some calculation on the corresponding line of pixels running parallel to the coating/substrate lines. Pixel values are linearly interpolated along columns when needed. These calculations are performed for all images in a given sequence, and the resulting columns of pixels are stacked horizontally from left to right to produce the condensed time-progression images, so that each successive column corresponds to a successive observation.

Plots were produced using the Matplotlib[18] package, and multipart figures were assembled using the ImageMagick[19] package.

3. RESULTS AND DISCUSSION

Following the procedures described above, we prepared four identical samples of each silica mixture formulation and performed drying observation experiments under different levels of IR heating power [0 W (ambient conditions), 50, 100, and 150 W]. We also prepared one sample of each NMC mixture formulation, which were dried only under the highest heating power of 150 W due to the relatively slow evaporation rate of NMP. We then processed all radiography image data collected during these experiments. We will briefly describe the processed images here, and below we present our interpretation of these data.

Figure 1 shows sample images, one from each of the four experiments using silica/AB/unmodified PAA/water/IPA mixtures with "medium" concentration (as defined earlier as having 70% liquid by weight) and conducted at four different heating powers. This figure is intended to provide readers with a sense of the effectiveness of the interface detection algorithm. In these images, interfaces have been artificially highlighted in red, and the air, coating, and substrate/platform are easily distinguishable. The compressed time-progression images discussed later will provide further assurance that the interface detection algorithm behaves in a reasonable way.

https://doi.org/10.1021/acsaem.4c00402
ACS Appl. Energy Mater. 2024, 7, 2989−3008

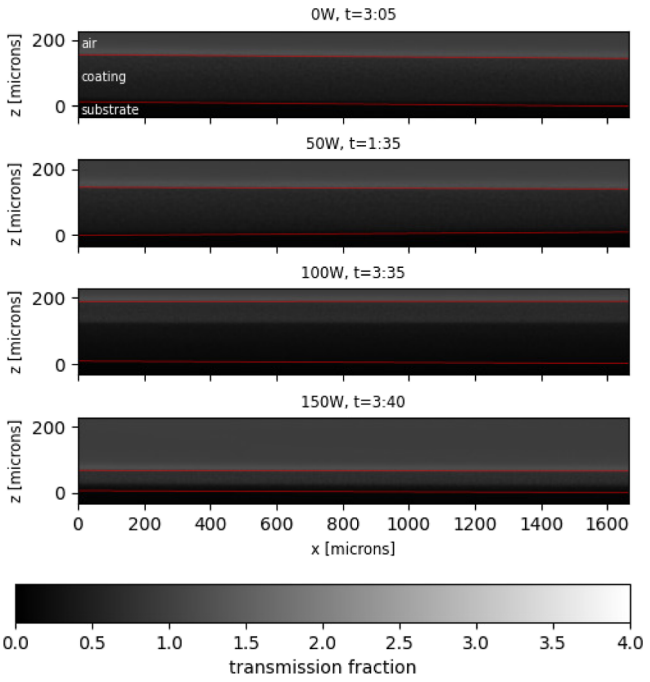

Figure 1. Images of coatings from medium-concentration, silica/AB/unmodified PAA/water/IPA experiments at different heating powers, at times of maximum apparent heights. Coating/substrate and air/coating interfaces were automatically detected and are artificially highlighted in red. The bright bands above the air/coating interface are phase contrast artifacts.

We observed that the height of the substrate unfortunately changes over time, even once the platform is in place for sample imaging. This is particularly evident in Figure S1, which shows the position of the coating/substrate interface relative to its initial position, with measurements taken at the horizontal centers of the images. We suspect that our experimental apparatus settles after each experimental setup, particularly so when heating power is applied, which will cause thermal expansion of various parts of the assembly; earlier in each experiment, the platform movement appears fairly insensitive to heating power, which we suspect is because the heating element temperature does not immediately rise to its steady operating value. It is challenging to control motions on the order of tens of microns in a portable assembly with a length scale of a meter, so the image processing procedure described earlier includes a step in which image sequences are aligned according by their substrate locations.

We also observed that it was necessary to realign the substrate/platform with the camera using the platform manual tilt-adjustment mechanism, prior to each experiment. The platform tilt-adjustment mechanism includes a complex, lubricated joint, and we suspect that the lubricating grease flows due to the weight of the platform, and likely more easily when heated. Furthermore, the platform is lifted off of the tilt-adjustment support to apply a foil substrate prior to each experiment, which is likely to redistribute the lubricating grease. Settling of the tilt mechanism is a concern because the platform plane and the X-ray beam must be well-aligned in order to prevent parts of the coatings from being blocked by the substrate/platform itself, as the substrate/platform edges extend beyond the edges of the coatings. We illustrate this in Figure S2, prepared using the Xfig[20] program, which contains diagrams (not to scale) of the coating, substrate, and platform. It is clear from these diagrams that when the platform is tilted relative to the X-ray beam, the edges of the substrate/platform can obscure parts of the coating. The copper foil substrate and aluminum platform both significantly limit X-ray transmission, so when these block the X-ray beam, the corresponding pixel values cross the image segmentation threshold used to distinguish coating and substrate/platform pixels. The small inset diagrams show that this would cause the apparent coating height, corresponding to the part of the coating that is visible above the edges of the substrate/platform, to be lower than the true coating height (although in reality, the edges of the coatings do not involve sharp right angles). Based on our suspicion that the platform tilt correction support is relaxing and settling, we expect that the platform will tilt clockwise (relative to the axes in Figure S2 and corresponding specifically to the middle diagram), potentially during observation. Increasing misalignment would cause reduction in apparent coating height.

The suspected platform tilt would prevent us from directly probing the full widths of coatings throughout the drying processes. Additionally, we lack tilt measurements and coating thickness maps. For these reasons, we are unable to produce estimated concentration profiles within the field of view, as we did in our earlier work.[7] We acknowledge that this presently limits us to a mostly qualitative examination of images. However, despite the suspected platform misalignment, we can extract some useful information from the images.

We plot the apparent coating heights as a function of time for the medium-concentration silica/AB/unmodified PAA/water/IPA samples in Figure 2, where we define the apparent height of a coating to be the perpendicular distance from the coating/substrate line to the air/coating line, taken from the coating/substrate line at the horizontal center of each image. The apparent coating heights observed at the start of each experiment, shortly after the samples are cast into coatings, are much lower than the doctor blade height of 400 μm due to some combination of fluid behavior and platform tilt. Over fairly large time intervals, these apparent heights then increase to much larger maximum values (the profiles at the maximum apparent coating heights were shown earlier in Figure 1). We will discuss this surprising behavior below.

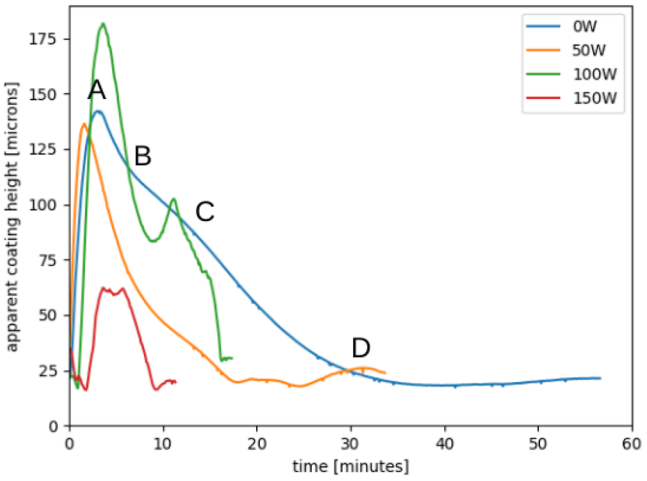

Figure 2. Apparent coating heights (taken at horizontal centers of images from substrate lines), during medium-concentration, silica/AB/unmodified PAA/water/IPA experiments with different heating powers.

https://doi.org/10.1021/acsaem.4c00402
ACS Appl. Energy Mater. 2024, 7, 2989−3008

In some of the experiments described in the present work, parts of the coatings (at the edges, based on later inspection of the samples) clearly delaminated from the substrate while under observation. Our automated image analysis procedure was not designed with delamination in mind, and in any case, delamination is an undesirable product outcome. For such experiments, our analyses and figures such as Figure 2 only include images collected prior to the instants at which we judged delamination to be clearly evident, based on radiography images.

The radiography images of coatings in the profile include information beyond apparent coating height. With radiography, the X-ray beam interacts with the entire width of the coating when the platform is well-aligned, so radiography cannot provide unambiguous information about coating variation along the direction of the beam. However, assuming that the coatings are reasonably consistent along this direction, one can examine coating variation in the perpendicular directions. Along the vertical direction, one can monitor variations in X-ray absorption as a proxy for vertical variation in concentration, which would be analogous to our approach in previous work.[7] However, since our experiments likely involve some unknown degree of platform tilt, each line of pixels parallel to the coating/substrate interface in a profile image might represent X-ray transmission along planes that are tilted with respect to the substrate surface and therefore intersect the coatings over a range of depths, preventing quantitative interpretation. Separately, along the horizontal direction, one could detect variation along the coating plane, which is of interest because an expectation of electrode coating fabrication is that uniformity promotes consistent product performance.

We have included pairs of condensed time-progression images, which were described above. Those collected for medium-concentration silica/AB/unmodified PAA/water/IPA samples for a range of heating powers are shown in Figures 3−6. Results for mixtures of the same materials at low and high concentrations are shown in Figures S3−S6 and S7−S10, respectively. Images for the silica/AB/Li-PAA/water/IPA mixtures are shown for a range of heating powers in Figures S11−S14. For silica/AB/Cs-PAA/water/IPA, these are shown in Figures S15−S18. Finally, for NMC/AB/PVDF/NMP, these are shown for different formulations in Figures S19−S24. The upper images in each of these figures are condensed time-progression images showing mean pixel values computed along lines running parallel to the substrate surface. The lower images in these figures are condensed time-progression images with pixel values representing the standard deviations divided by means, computed along the same lines. The latter describe coating consistency along the horizontal direction and tend to highlight the interfaces—in general, it is apparent from these images that variability is highest at interfaces, at which we expect to see phase contrast artifacts due to X-ray refraction. Readers might find the lower images to be helpful in guiding the eyes to some of the interface behavior that we will discuss. Otherwise, these images do not show large irregularities within the drying coatings, suggesting that the plots of mean values generally provide reasonable representations of coating evolution.

The horizontal scales differ among these condensed time-progression images because they accommodate the differing time intervals over which the different experiments were run. As mentioned above, for each image, the end of the coating/substrate line that is closest to the image bottom is assigned a height of zero. Calculations are performed along lines that are parallel to the detected coating/substrate lines. With this

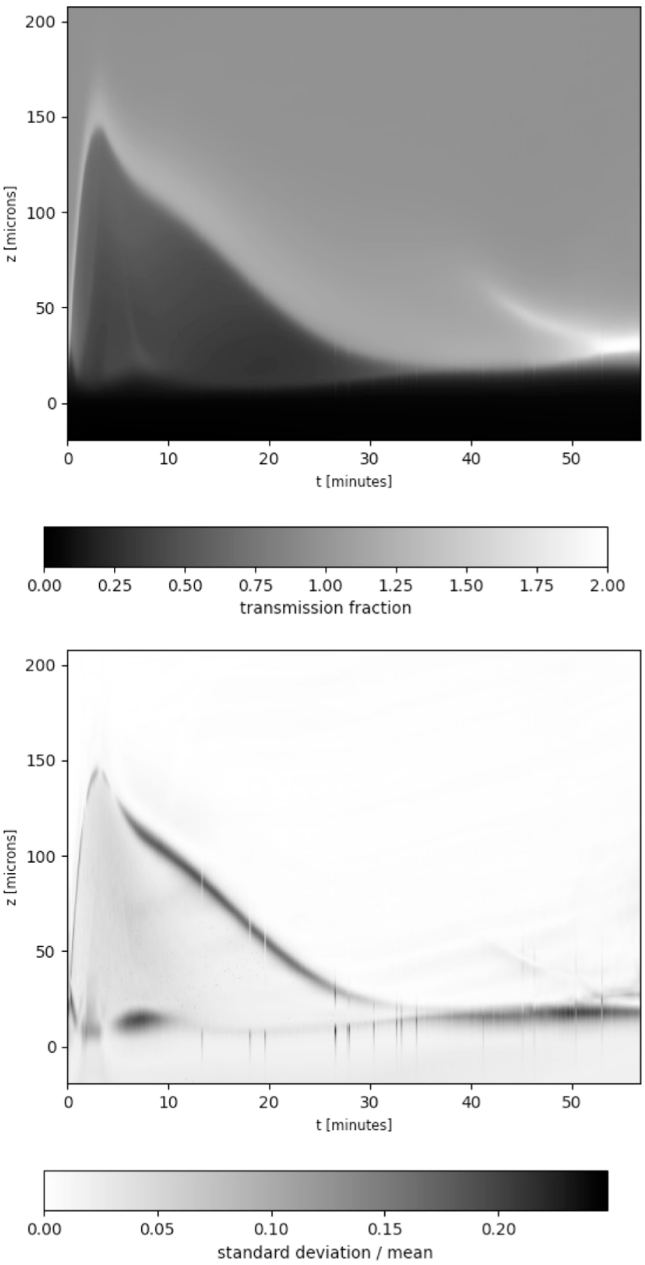

Figure 3. Condensed time-progression images (see description in text) generated from the 0 W image sequence for medium-concentration, silica/AB/unmodified PAA/water/IPA sample. Top: mean transmission fractions. Bottom: standard deviations divided by means.

arrangement, all pixels below $z = 0$ ideally correspond only to the substrate (and parts of the coating obscured by a tilted substrate), and all pixels above $z = 0$ ideally correspond to the coating or air. The apparent coating height curves for the medium concentration silica/AB/unmodified PAA/water/IPA samples, shown earlier in Figure 2, correspond to the readily visible air/coating interfaces in condensed time-progression images (Figures 3−6). The bright layers just above the air/coating interfaces are artifacts resulting from X-ray refraction, and we suspect that the bright curves far above the air/coating interfaces are from X-ray reflections off of the apparatus, which settles slightly throughout the experiments, as we noted earlier.

The NMC/AB/PVDF/NMP mixtures were clearly more viscous than the medium concentration silica/AB/unmodified

https://doi.org/10.1021/acsaem.4c00402
ACS Appl. Energy Mater. 2024, 7, 2989−3008

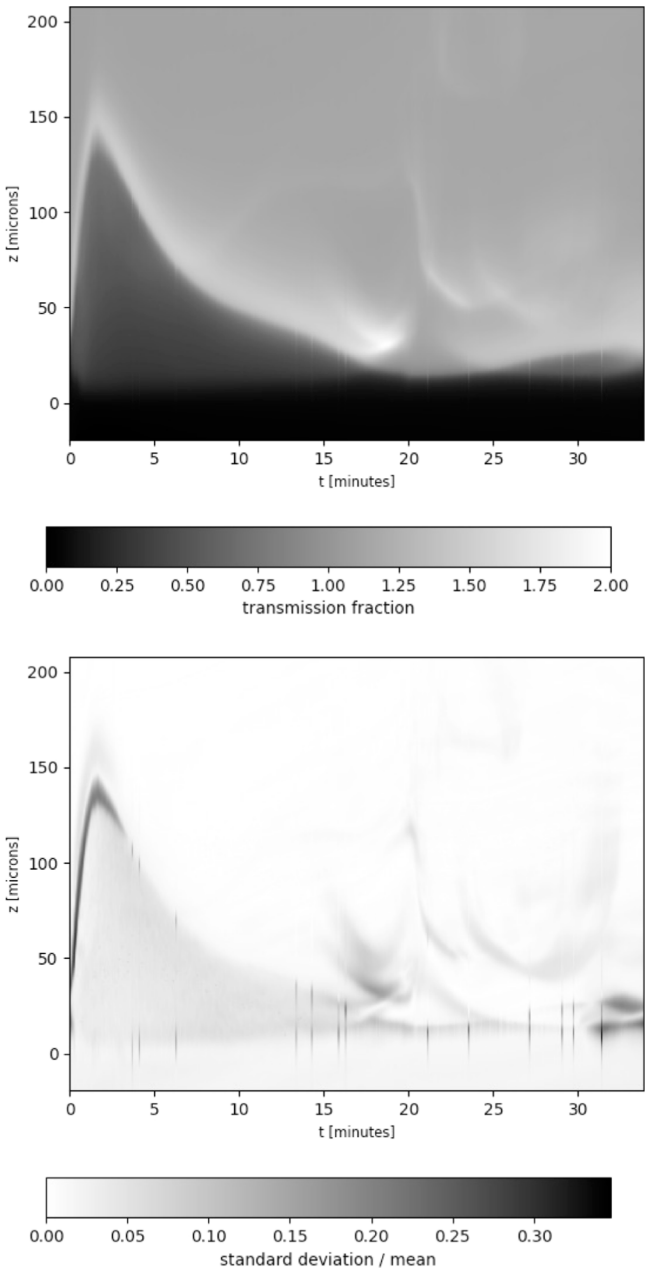

Figure 4. Condensed time-progression images (see the description in text) generated from the 50 W image sequence for medium-concentration, silica/AB/unmodified PAA/water/IPA sample. Top: mean transmission fractions. Bottom: Standard deviations divided by means.

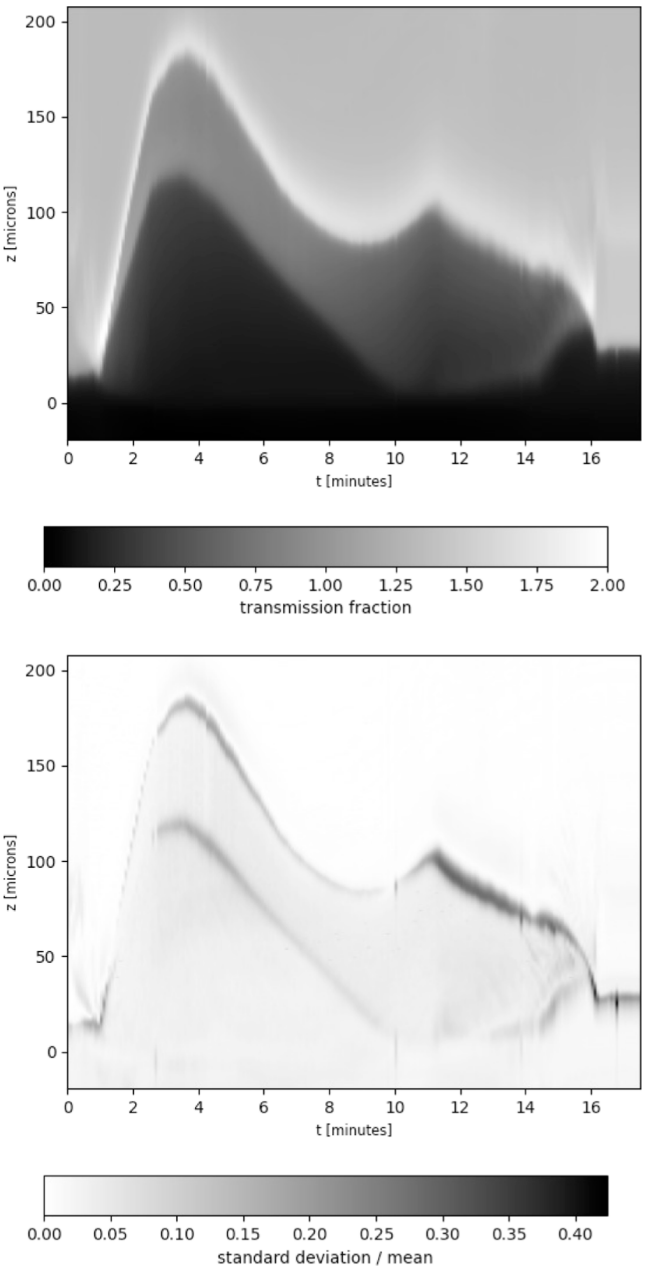

Figure 5. Condensed time-progression images (see description in text) generated from the 100 W image sequence for medium-concentration, silica/AB/unmodified PAA/water/IPA sample. Top: mean transmission fractions. Bottom: standard deviations divided by means.

PAA/water/IPA mixtures, based on our experiences in dispensing them prior to casting. Figures S19 and S22 show condensed time sequences for the medium-concentration mixtures from the "low AB" and "high AB" experiments (both defined above). The amount of NMP was also higher in the high AB mixture than in the low AB mixture, so the high-AB mixture was not necessarily more viscous. We generated these images by applying the same interface detection algorithm and thresholds used with the results from our experiments with silica particles. Unfortunately, NMC is much less transmissive to X-rays than is silica, so image contrast is poor and it is difficult to see details within the coatings. However, the changes observed during the drying processes of the NMC/AB/PVDF/NMP mixtures are clearly far less dramatic than with the earlier, less viscous low-concentration and medium-concentration mixtures of silica/AB/unmodified PAA/water/IPA.

To supplement the image data, we collected micrometer measurements of the dried coatings at a variety of positions: near the "leading" edges of the coatings (closest to the initial doctor blade position), near the centers of the coatings (closest to the radiography field-of-view and away from all edges), near the "trailing" edges of the coatings (closest to the final doctor blade position), and for only two of the silica/AB/unmodified PAA/water/IPA mixtures, along the sides perpendicular to the X-ray beam. For coatings produced from medium and high concentration silica/AB/unmodified PAA/water/IPA mixtures, these measurements are provided in Tables S1 and S2,

https://doi.org/10.1021/acsaem.4c00402
ACS Appl. Energy Mater. 2024, 7, 2989−3008

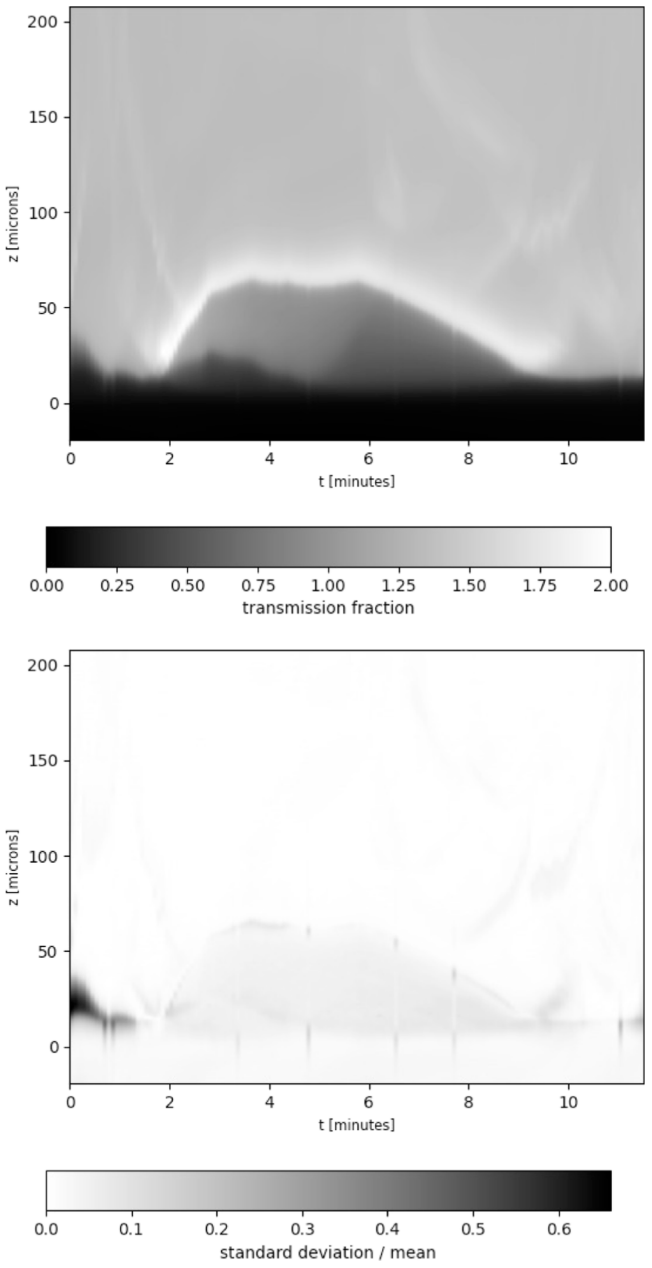

Figure 6. Condensed time-progression images (see description in text) generated from the 150 W image sequence for medium-concentration, silica/AB/unmodified PAA/water/IPA sample. Top: mean transmission fractions. Bottom: standard deviations divided by means.

respectively. We have not provided micrometer measurements of the dried coatings cast from the low concentration mixtures or in the 0 and 50 W experiments with medium concentration mixtures, all of which delaminated from the substrates when handled during removal from the apparatus. For medium concentration silica/AB/Li-PAA/water/IPA mixtures, measurements are provided in Table S3. For medium concentration silica/AB/Cs-PAA/water/IPA mixtures, measurements are provided in Table S4. For all NMC/AB/PVDF/NMP mixtures, measurements are given in Table S5. We will discuss these results below. However, we first note that the lowest dry coating heights measured for the coatings produced from the medium concentration silica/AB/unmodified PAA/water/IPA mixtures are substantially higher than the apparent long-time (presumably, dry) coating heights shown earlier in Figure 2, which is consistent with significant platform tilt for this set of experiments.

We now discuss each sample set in further detail.

3.1. Medium-Concentration Silica/AB/Unmodified PAA/Water/IPA Samples. Our discussion of this sample set will cover a wide range of behavior and will serve as a reference point for later discussion of the other sample sets.

We first note that the apparent final coating heights seen in Figure 2 are similar to each other, but as mentioned above, these are substantially smaller than the similar thickness values given for the two samples described in Table S1. We conclude that the platform tilt has reached similar limits toward which the apparatus settled during each experiment; later, we will highlight evidence that suggests that the progression of platform tilt has stopped prior to or shortly after the start of imaging in all experiments. We also see that despite the similarities among substrate surface positions early in each experiment (Figure S1), these positions cannot be taken to be reliable indicators of platform tilt, since at least at later times, there is wide variation in relative substrate height despite similar apparent final coating heights (Figure 2) and similar dry laminate thicknesses (Table S1).

As noted earlier, the large apparent height increases shown in Figure 2 are particularly surprising. Why might these occur? Platform tilt progression should cause apparent heights to decrease, as suggested by Figure S2. Solvent evaporation should eventually cause apparent heights to decrease. The only remaining influence that is plausible to us is fluid flow.

Based on experience, we exclude the possibility of fluid redistribution and height change due to changes in coating area. We have not observed the edges of coatings to move significantly after casting, so although we have observed coating heights to evolve over a time scale of minutes, the edge positions of coatings established through casting actions remain as boundaries for the fluids. As a demonstration of this, we have provided Figure S25, which shows a sample of the same formulation dried under ambient conditions for 36 min, in this case on an aluminum foil surface. A camera in a fixed position was used to photograph the sample at the beginning and end of the experiment, and two images were produced by pixel-by-pixel subtraction of the first image from the second and the second image from the first, with negative values adjusted to zero (that is, shown as black pixels). The aluminum substrate is brighter (that is, it has a larger grayscale pixel value) than the sample. If the sample edges were to expand or recede over time, we would then expect to see a bright ring along the edge of one of these images. Since no such ring is apparent in either of the images, we conclude that the coating edge for this sample was stationary at this scale, even for a sample such as this, which flows relatively freely in comparison to some of the later samples that we will examine. The location of the coating edge must significantly influence the coating height, area, and thickness, and the active material loading.

We can envision two remaining possibilities for fluid redistribution within a coating leading to significant increases in height:

1 .The coating might become more uneven over time through fluid flow along the direction of the beam. Although gravity will tend to flatten the coating, we might anticipate that thickening would occur near the coating edges because the coating height must decrease to zero at

https://doi.org/10.1021/acsaem.4c00402
ACS Appl. Energy Mater. 2024, 7, 2989−3008

the edges but surface tension would resist the presence of sharp curves. As radiography provides only a profile projection through the entire coating width (under ideal circumstances, when the platform is well-aligned with the X-ray beam), the coating would appear to thicken, although the thickening edges would draw fluid from the interior of the coating, making the interior thinner.

2 .Fluid flow along the coating direction, perpendicular to the beam, could deliver fluid into the field of view (located approximately at the horizontal center of the coating, between the leading and trailing edges). We can imagine two causes for this, although we are presently unable to distinguish between them:

   (a) The coating might be uneven along the coating direction, and relaxation toward uniform coating height could occur through fluid flow. This would require an excess of fluid volume outside of the field of view, closer to the leading or trailing edge of the coating.

   (b) The passing doctor blade might impart some momentum to the fluid outside of the field of view, causing material closer to the leading edge to eventually flow into the field of view, and perhaps causing material within the field of view to flow out.

Considering the two hypothetical flow direction scenarios, we now examine the thickness measurements obtained for the dried laminates from the 100 and 150 W experiments (see Table S1):

1 There is some unevenness along the direction of the X-ray beam, with the sides of the coatings indeed somewhat higher than at the centers. However, the peak apparent heights in Figure 2 are significantly higher the initial heights. In this scenario, material would have moved from the center to the edges, so at the moment of peak apparent height, the height in the interior would be lower than the initial height, and the heights of the edges would be significantly higher. Assuming that relative heights throughout the wet coatings are approximately reflected in the dry coatings, the relatively small differences in the micrometer measurements shown in Table S1 appear to exclude the first flow direction scenario.

2 While these dried laminates are also somewhat thicker near the trailing edges than at the centers, they are even thicker near the leading edges (Table S1). This is consistent with the second scenario, with the casting process initially leaving excess material near the leading edge. The excess material might then flow to the rest of the coating due to some combination of gravity and momentum, but might not have enough time to relax fully before drying. In Figure 7, we have provided a diagram (not to scale), prepared using Xfig,[20] which illustrates this scenario. Coating height nonuniformities might not relax fully before fluid flow stops due to solvent evaporation; Figure 2 suggests that this fluid flow along the casting direction occurs on a time scale of minutes in these experiments.

We acknowledge that this flow behavior might be specific to lab-scale casting processes and might depend strongly on casting conditions, such as coating speed and doctor blade construction, although we have not explored these possible influences in this work. Industrial casting processes typically involve roll-to-roll lines which might use, for instance, slot-die or slide-die techniques. Casting would ideally occur under continuous,

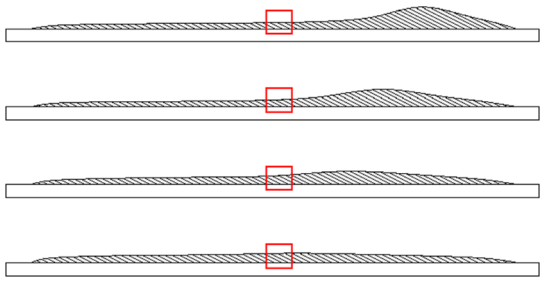

Figure 7. Illustration of flow due to relaxation of excess fluid, not drawn to scale. One could take the red boxes to represent the field of view. During the casting process, the doctor blade here left an excess of material outside of the field of view. Not shown is volume loss through ongoing solvent evaporation.

steady-state conditions and produce coatings of uniform height in the coating direction. In our case, steady-state conditions are clearly not met when the doctor blade first encounters a mixture sample or leaves the trailing end of a coating. Additionally, while we did not make viscosity measurements, when dispensing samples, it was readily apparent that the more concentrated samples were more viscous than the less concentrated samples, and viscosity appeared to have a significant influence on the flow behavior, as we will discuss later.

We now examine the behavior at later times, also shown in Figure 2. Toward the end of each experiment, the apparent coating heights (Figure 2) are fairly stable, which we expect to correspond to dry or nearly dry coatings, although we anticipate that some thermal expansion might occur under continued heating. Working backward, at intermediate times, we expect that the observed apparent coating heights are influenced by several factors:

1. Based on our platform construction, we expect that platform tilt will progress in a clockwise orientation (from the perspective of Figure S2), which will tend to decrease apparent coating height. As discussed earlier, it appears that there is a limit for platform tilt that is reached by the end of each experiment. Furthermore, due to limitations in our platform alignment procedure as well as the time delay between sample setup and observation, the platform might be tilted at the start of observation. When starting from a counterclockwise orientation and proceeding to a clockwise orientation, we would expect to observe apparent coating height to first increase to the true coating height as the platform becomes well-aligned and to later decrease as the tilt progresses in clockwise orientation.
2. As fluid is redistributed within the coatings, fluid flow rates within the coatings should vary over time. Some of the unevenness in coating height will be preserved as neighboring material flows in and out of the field of view, and whether fluid motion is primarily driven by relaxation of an excess of fluid toward the leading edge of a coating, or by momentum imparted through the earlier passing of the doctor blade, the fluid flow is not a steady-state process. Additionally, we expect that the flow will encounter little initial resistance as the fluid "front" moves unimpeded toward the trailing end of the coating. However, as mentioned earlier, the initial coating boundaries do not move significantly after casting in our experience. After the fluid front reaches the trailing edge of a coating and is unable to progress farther, fluid should

https://doi.org/10.1021/acsaem.4c00402
ACS Appl. Energy Mater. 2024, 7, 2989−3008

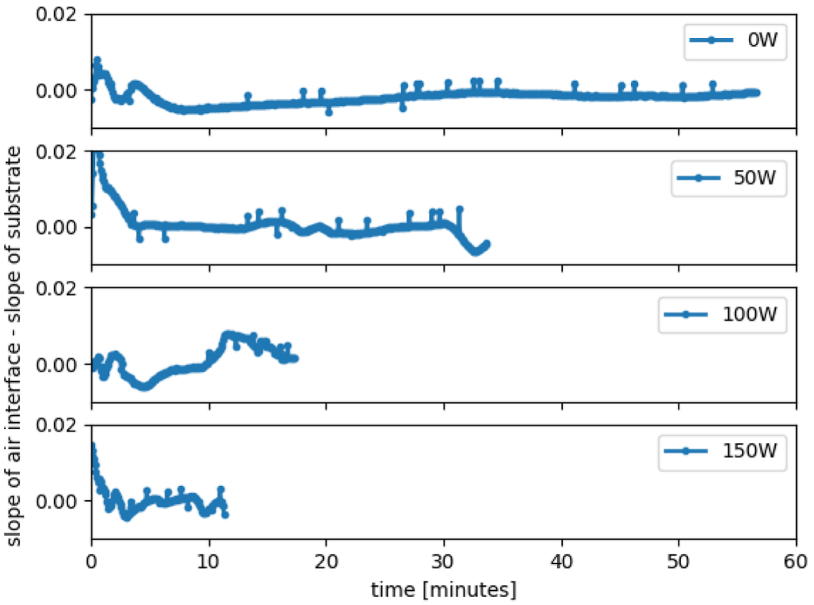

Figure 8. Difference of slopes of air/coating and coating/substrate interfaces, during medium-concentration, silica/AB/unmodified PAA/water/IPA experiments.

flow in a qualitatively different way, and the influence of this boundary should propagate backward toward the leading edge. Finally, appreciable fluid flow might stop long before a coating is fully dry.

3. We expect that solvent evaporation will usually decrease coating height, although the relationship between solvent evaporation and coating height and structure might become complicated near the end of the drying process.[21] We also expect the influence of solvent evaporation to continue after there is no longer appreciable fluid flow, when the coating might be thought of as a damp solid rather than a complex fluid; since we were able to observe parts of the coatings through the beamline hutch window and stop experiments after the visible regions appeared dry, we expect that solvent evaporation was the last major influence to wane in our observations.
4. Temperature increases from heating will subtly increase coating height through thermal expansion. We expect this effect to be gradual at early and intermediate times, with potential for an abrupt change in influence when a coating is nearly dry.

All of these influences might be in effect from the start of observation, but we see no reasons for multiple influences to wane at exactly the same times, so we expect to notice behavior in which one influence stops but other influences continue. The apparent coating height curves from the 0 and 50 W experiments indeed show regions of differing slope after reaching peak apparent height.

With the above influences in mind, we now reexamine the 0 W curve (that is, with the heater turned off) from Figure 2. After reaching its peak apparent height, the 0 W curve shows:

1. a steep slope (high rate of apparent height decrease),
2. followed by a transition (at around 5 min) to a shallower slope (lower rate of apparent height decrease),
3. followed by a transition (at around 13 min) to a steeper slope,
4. followed by a transition (at around 30 min) to fairly static behavior at later times.

Considering the mechanisms proposed earlier, we work backward through the above transitions so that we introduce one influence at a time.

1. The nearly static behavior observed late in the experiment corresponds to a fully dry coating or a nearly dry coating from which further solvent evaporation ought to be relatively slow as remaining solvent must escape from a porous region with high solids concentration.
2. Since the nearly static region corresponds to a dry or nearly dry coating, we infer that the preceding transition (labeled as "D" in Figure 2) corresponds to the end of an interval in which apparent height change is almost entirely due to solvent evaporation, and during which there is not enough solvent to allow for appreciable fluid flow. Over much of this time interval, the rate of apparent coating height change is roughly constant, suggesting a roughly constant evaporation rate and that concentration changes in the coating during this time have little effect on the evaporation rate.
3. Traversing the preceding slope transition (labeled as "C"), one sees an acceleration in the rate of height decrease. We cannot attribute this to an increase in the evaporation rate, following the transition; due to ongoing solvent evaporation, we expect the coating to be less concentrated at earlier times, potentially exposing more solvent at the air/coating interface, so we further expect that the solvent is evaporating at least as quickly prior to the transition as after the transition. Our remaining explanation for volume change is that fluid is being supplied to the field of view through fluid flow prior to the transition, limiting the net decrease in coating height. The transition would then correspond to the end of appreciable fluid flow.
4. Traversing the first slope transition (labeled as "B") following the peak (labeled as "A") corresponds to a deceleration in the rate of height decrease, following the transition. We again see no reason for the evaporation rate to decrease abruptly, and while this deceleration might

https://doi.org/10.1021/acsaem.4c00402
ACS Appl. Energy Mater. 2024, 7, 2989−3008

indicate the end of platform tilt progression, evidence that we will present later in this discussion suggests that platform tilt tends to reach its limit much earlier in all experiments. Our only remaining explanation for the deceleration is that, in the interval from "A" to "B," fluid is not accumulating in the field of view at as high of a rate as it does prior to the peak or after this transition. As described earlier, the large increase in height prior to the peak appears to correspond to a fluid front moving across the coating and passing through the field of view, which we attributed to some combination of relaxation of an uneven surface (we suspect that mixtures with relatively low viscosity can escape under the passing doctor blade) or momentum imparted by the passing doctor blade. At the same time, solvent is evaporating from the entire coating surface. The peak "A" corresponds to the point in time at which the rate of fluid accumulation in the field of view changes from positive to negative, presumably due to some combination of net flow and evaporation rate. We will next discuss the potentially complicated fluid flow behavior between the start of the experiment and time "B."

For the present sequence of experiments with varied heating powers, we have plotted the difference of the slope of the air/coating interface and the slope of the coating/substrate interface in Figure 8 to provide additional context. The results appear to show significant noise, so we have reduced the number of points plotted in order to avoid visually obscuring the overall trends. We remind readers that the leading edges of the coatings are to the right of the field of view, so that a positive slope difference indicates that the coating is thicker toward the leading edge than the trailing edge within the field of view. Since our direct observations are limited to the narrow field of view, we are unable to determine whether momentum or relaxation under gravity of excess fluid is the primary driver of fluid flow here. If fluid flow is mostly driven by momentum, one might imagine observing features of a potentially uneven coating surface as it flows through the field of view. If fluid flow is driven largely by relaxation, we expect fluid to flow from thicker to thinner regions of the coating, so we would expect to see a positive slope difference if a fluid front traveling toward the trailing edge were to pass into the field of view.

The 0 W plot in Figure 8 initially shows a positive slope difference, which then becomes negative as the fluid height nears the peak, then positive in the immediate vicinity of the peak, and then negative again for an extended period of time. These changes could simply reflect the uneven height profile of the coating surface passing through the field of view with momentum imparted earlier by the passing doctor blade. Alternatively, for an uneven coating, one might imagine net flow from relaxation of excess fluid outside of the field of view, with simultaneous spreading of local excesses of fluid relative to the bulk of the excess fluid. We have illustrated such a scenario in Figure 7 and will later present an observation of local relaxation, although using a different sample formulation. In the illustrated scenario, the center of the fluid excess passing through the field of view would appear as a change in sign of the slope difference, from positive to negative, although this simple scenario would not explain the multiple changes in slope difference in the 0 W experiment (Figure 8). However, one might further imagine that inconsistencies in coating processes could leave multiple excesses of fluid on either side of the field of view and at different distances to the field of view, or fluid excesses which contain smaller local excesses of fluid. Simultaneous relaxation of all of these excesses could result in multiple fluid fronts and multiple changes in sign of the slope difference in the field of view. Additionally, when the evaporation rate is sufficiently low, we expect fluid fronts to eventually encounter additional resistance that will prevent them from flowing freely, whether driven primarily by momentum or relaxation. A fluid front might encounter another fluid front relaxing in the opposite direction or might reach the far end of the coating; as noted earlier, the coating boundaries do not change appreciably after casting, and so act as boundaries to fluid flow. If fluid is prevented from flowing as freely, it will reside for longer in other coating regions, increasing local rates of accumulation. We suspect that such a qualitative change in flow behavior is responsible for the slope transition "B" in Figure 2, although we are limited by our direct observations being confined to the field of view. Furthermore, one might suspect that early momentum-driven flow of fluid from one edge to the other might itself create obstacles to further flow by causing an excess of fluid to temporarily build up near the second edge, leading to later relaxation of the excess fluid toward the first edge. For example, slope differences in the 0 W experiment are negative over a long interval at later times (Figure 8).

We now examine the cases involving IR heating. The 50 W curve in Figure 2 appears to have a qualitatively similar structure to the 0 W curve. The apparent coating height curve passes through a peak at around 4 min and slope transitions at around 7, 15, and 18 min. The variation in coating height late in the experiment might reflect coating movement due to thermal stresses and subtle delamination, which we will not examine. However, for this experiment, the plot of slope differences in Figure 8 is particularly simple. It shows positive values at earlier times and later decreases to zero, and the values remain near zero for the rest of the experiment (the changes at the very end of the experiment are unlikely to correspond to fluid flow and might indicate changes such as subtle delamination). However, we are hesitant to perform a quantitative comparison with the 0 W results because the use of the heater in the 50 W case will hasten evaporation, which should increase fluid viscosity and reduce fluid velocity, if all else were equal. One could interpret these results as simply corresponding to a plateau of fluid relaxing and moving through the field of view toward the trailing edge, although the qualitative similarities with the 0 W plot suggest that the same mechanisms might be at work. It would be quite coincidental for a distribution of multiple relaxing fluid excesses producing the changes in slope difference seen in the 0 W curve in Figure 8 to also cause coating height to evolve in a similar way as with the relaxation of a single excess of fluid (comparing the 0 and 50 W cases in Figure 2). For this reason, we suspect that the apparent coating height changes in these experiments are primarily driven by fluid momentum. We again attribute the peak in apparent height to some combination of fluid accumulation and evaporation, and the slope change (Figure 2) at 18 min to the end of significant solvent evaporation. The changes at 7 at 15 min do not clearly correspond to features in the plot of slope differences (Figure 8), which again causes us to doubt that the observed changes in apparent coating height are primarily driven by relaxation. As in the 0 W case, we suspect that these changes correspond to a change in fluid flow due to the influence of the trailing edge and the end of appreciable fluid flow, respectively.

https://doi.org/10.1021/acsaem.4c00402
ACS Appl. Energy Mater. 2024, 7, 2989−3008

Returning to Figure 2, we see that unlike the 0 and 50 W curves, the 100 W curve has a second peak and an abrupt transition to a stable apparent height signaling the end of the experiment. In contrast with the 0 and 50 W cases, the slope difference for the 100 W curve (Figure 8) varies over negative and positive values for most of the time leading up to the peak apparent height, despite the early increase in height appearing qualitatively similar. This again causes us to suspect that the early fluid flow behavior reflects an uneven surface driven by momentum. However, unlike with the 0 and 50 W cases, the apparent height in the 100 W case shows a second peak at a later time. The latter peak appears to coincide with a peak in the slope difference, so we suspect that this peak is due to relaxation of excess fluid, as we hypothesized earlier, with evaporation causing the fluid to become more viscous and eventually halting the flow. The positive slope difference values suggest that the excess fluid was initially quite far from the field of view, and toward the leading edge of the coating. That the initial distribution of fluid was apparently somewhat different from that in the 0 and 50 W experiments is not surprising, given the inconsistency inherent in our manual sample deposition process.

The 150 W curve in Figure 2 appears to be quite different from the others. As we will address later in this discussion, our observations suggest that the sharp early drop in apparent coating height corresponds to progression of platform tilt, which reaches its limit before the fluid flow stops. Unlike in the other experiments, the 150 W curve shows a plateau rather than a clear single peak in apparent coating height, which might suggest that some of the slope difference transitions described earlier occurred very closely in time, or might not have occurred at all due to rapid solvent evaporation and halting of flow; comparison with the previous experiments suggests that the fluid flow ended relatively early. While the plot of slope difference values (Figure 8) is reminiscent of the 50 W plot and might be interpreted as relaxation of the excess fluid, we again suspect that the early rise in apparent height is primarily momentum-driven since the same mechanism would more easily explain the 0 and 100 W plots as well. Returning to Figure 2, the slope beyond the plateau does not show a transition until the drying process is complete, at around 10 min, and should correspond primarily to solvent evaporation. This transition is abrupt, as in the 100 W case. That the resulting coating is similar in thickness to the other coatings suggests that despite the differences in apparent height dynamics, roughly the same area density of solid material was deposited, so the flowing fluid was relatively concentrated.

We now discuss the condensed time-progression images for this set of samples (Figures S3−S6). With the present mixture composition, the parts of the coating that have the highest concentration of silica particles are expected to transmit the least amount of light. The substrate/coating interfaces have been placed at $z = 0$ using the image analysis procedure described earlier. Although we expect pixels below $z = 0$ to be dark, indicating poor transmission through the substrate, dark regions clearly extend above $z = 0$ in all of these images, starting at $t = 0$. We suspect that the dark regions above $z = 0$ are particle-rich regions formed through rapid settling in the time between casting and collection of the first radiography images, and we will refer to these as "high-density" regions. The air/coating interfaces are readily visible and coincide with the plots of apparent height in Figure 2, and their bright outlines are phase-contrast artifacts from radiography imaging. The gray regions above the high-density regions and below the air/coating interfaces are less concentrated coating regions, which we will refer to as "low-density." We acknowledge that we are making these classifications of coating regions on the sole basis of initial appearance. We also note that the platform is positioned for observation about half a minute after the coating is produced, and the existence of the high-density regions so soon after casting is in conflict with many drying and consolidation models.[21] We suspect that the high-density regions primarily contain relatively large particles for which Brownian forces have limited influence, and that the low-density regions primarily contain relatively small particles with colloidal behavior.

We first examine the 0 and 50 W images (Figures 3 and 4), which appear to be similar. The high-density regions remain fairly uniform in apparent height despite substantial changes in the heights of the low-density regions during the same time intervals. We have used fluid flow to explain much of the changes in apparent coating height. These images suggest that the low-density regions here flow much more freely than the high-density regions, which is consistent with our expectation that the more concentrated high-density regions are more viscous than the low-density regions. Some readers might find that interfaces between some regions are easier to see in the lower images showing standard deviations divided by means than in the upper images showing mean values; larger values in the lower images can arise when interfaces are not sharp or are not perfectly aligned with the substrate. Additionally, in both Figures 3 and 4, the high-density regions tend to increase slightly in apparent height at later times as the low-density regions rapidly decrease in apparent height, as one might expect for a particle-laden fluid coating that is drying and consolidating into a solid coating. The high-density regions that were present from the start of observation appear to make up substantial fractions of the final coatings at the end of their drying processes. Finally, the appearances of lighter regions above the high-density coatings near the end of the experiments might indicate subtle delamination of parts of the coatings, viewed in profile.

Looking very closely at Figures 3 and 4, one can see sharp initial decreases in the apparent heights of the high-density regions. These do not seem to be caused by fluid flow because the heights of the high-density regions are fairly stable over much of the intervals over which the apparent coating heights later increase dramatically due to fluid flow. Instead, we suspect that these sharp decreases in the heights of the high-density regions show progression in degree platform tilt. Additionally, the apparent heights of the high-density regions are fairly stable at later times in both of these experiments. While platform tilting might have started during each experiment before radiography images were collected, these images suggest that changes in platform tilt continued only briefly after the start of image collection in both experiments.

One can see that transmission through the low-density regions of the 0 and 50 W coatings (Figures 3 and 4) changes fairly gradually with vertical position. However, the corresponding images for the 100 and 150 W experiments, shown in Figures 5 and 6, clearly show development of two layers within the low-density regions soon after the onset of fluid flow, presumably with silica particles more concentrated in the lower layer. We will use the term "stratification" to refer exclusively to this development of layers within the low-density region. Lighter layers emerge at the tops of the low-density regions in both cases. Since this stratification is only observed at the higher heating powers, we conclude that it is primarily driven by heating rather than by gravity. At lower heating powers, we do not see this stratification despite the longer drying times

https://doi.org/10.1021/acsaem.4c00402
ACS Appl. Energy Mater. 2024, 7, 2989−3008

providing the relatively dense silica particles with more opportunity to settle before the end of each experiment. It is well-known that temperature gradients can produce mass fluxes (the Soret effect[22]), and we expect that most of the IR radiation will be absorbed by material closer to the coating surfaces. These layers are also visible in the 100 and 150 W images shown in Figure 1, which shows the coatings in profile at the moments of maximum coating height.

The image sequences in Figures S26 and S27 show this development of stratification in the form of coating profile images. The low-density regions start as single darker layers, and lighter layers soon emerge. The lighter layer grows more slowly in the 100 W experiment than in the 150 W experiment, which we expect as a consequence of the lower heating power. Also in both cases, the high-density regions appear to decrease slightly in thickness when the overall apparent coating heights begin to increase due to fluid flow. We suspect that the fluid flow is agitating some material at the top of the high-density region and mixing it into the low-density region.

In both the 100 and 150 W experiments, the lower layers within the low-density regions decrease in thickness over time and disappear (Figures 5 and 6); they cannot be merely obscured due to platform tilt because the upper layers within the low-density regions are more transmissive. At around the times that these lower layers disappear, the upper layers appear to become less transmissive. We suspect that this is primarily due to replacement of material within the field of view with more concentrated material by fluid flow, since darkening begins before the apparent coating height decreases. For the same reason, we cannot attribute this primarily to increasing concentration due to solvent removal. Also, we do not see simultaneous reduction in the apparent thickness of the high-density region, so we cannot explain this based on agitation of material from the underlying high-density regions. Finally, while this decrease in transmission occurs fairly uniformly throughout the low-density region in the 100 W experiment, it emerges as a new lower layer in the 150 W experiment and gradually increases in height as the upper layer thins and vanishes; although this might seem inconsistent with material replacement because fluid should move most freely near the free coating surface, this could be explained by the incoming flow having a vertically nonuniform distribution of silica.

Also, the condensed time-progression image for the 150 W experiment, shown in Figure 6, provides further support for our suspicions surrounding platform tilt and high-density regions. The image suggests that the coating in the field of view initially consists entirely of a high-density region that soon decreases in apparent height to a nearly stable level, long before the increase in apparent coating height caused by fluid flow. We do not expect the high-density regions to flow readily, so we suspect that this fairly rapid change in height corresponds to the platform continuing to tilt until it has reached some limit.

Finally, we found that the dried laminates produced in the 100 and 150 W experiments (Figures 5 and 6) were mechanically robust, while those produced in the 0 and 50 W experiments (Figures 3 and 4) readily delaminated upon handling. Here, samples showing stratification were the same ones that possessing good coating adhesion. It is possible that the influence of heating on material distribution, such as concentration of binder near the substrate, was critical to coating adhesion. However, a high-density region, presumably also containing a relatively high density of binder, was present in all of these experiments, so we believe that heating influenced adhesion through some other mechanism, such as through elongating polymer chains.

It can be difficult to visually match pixel values and color bars in the condensed time-progression images. To aid in further interpretation, we have also plotted pixel values indicating mean transmission fraction as a function of height at selected times, which correspond to columns in the condensed time-progression images. The plots corresponding to Figures 3−6 are shown in Figures S28−S31.

We first examine the 0 W plots (Figure S28). At the top of the plot, all curves approach a transmission fraction of slightly less than 1. One might expect a value of 1 to correspond to the unobstructed background. However, the point spread function of the scintillator results in a low-intensity, large-area glow. Therefore, images in which the sample platform obstructs a large part of the scintillator (that is, all of our images of samples) have slightly lower average values in unobstructed regions than do the background images with no obstructions. As one then looks down toward the air/coating interface, the transmission fraction increases to higher values, corresponding to phase contrast artifacts resulting from X-ray refraction. Looking across the air/coating interface into the coating, the transmission fraction values decrease sharply; in general, readily visible interfaces in condensed time-progression images correspond to nearly horizontal sections of these transmission fraction curves. Below the interface is the low-density region of the coating, within which the plots show gentle gradients, perhaps in part due to mild gravity-driven concentration gradients. We would ideally use these pixel values to estimate concentration as in our earlier work,[7] but the unknown degree of platform tilt prevents us from assigning average linear absorption coefficients to coating material in planes parallel to the substrate. Still, the pixel values show reduced transmission over time, which we expect from the low-density region becoming more concentrated due to solvent evaporation. The increase in pixel brightness observed at later times in the thinning low-density region might correspond to phase-contrast artifacts. At the interface between the low-density region and the high-density region, we again see the curves become nearly horizontal. The similarity among all of the curves as they near $z = 0$ suggests that the concentration profile in the high-density region is quite consistent over the range of times shown, perhaps with the exception of material toward the top of the high-density region, which might be relatively dilute and which might be somewhat agitated by flow in the adjacent low-density region. Finally, the values below $z = 0$, corresponding to the substrate, are quite consistent as we should expect. We remind readers that the choice of a pixel value threshold distinguishing the substrate/platform from all other regions was somewhat subjective. Nevertheless, the consistency of these plots provides further assurance that our image processing procedure behaves in a consistent and reasonable way.

Unlike in the 0 case, the 50 W curves (Figure S29) show a transmission fraction gradient within the coating that becomes significantly more severe over time. Presumably, the heating is making this gradient more severe, but not enough to produce stratification as at higher heating powers. As in the 0 W case, the curves each have two nearly horizontal regions, corresponding to the air/coating interface and to the interface between the low-density and high-density regions. The curves in the high-density regions are quite consistent, which suggests that the high-density region retains its character over the time interval shown, despite very visible changes in the low-density region, as one might guess

https://doi.org/10.1021/acsaem.4c00402
ACS Appl. Energy Mater. 2024, 7, 2989−3008

from its consistent appearance in the corresponding condensed time-progression image (Figure 4).

Recalling the 100 W condensed time-progression image (Figure 5), the flowing fluid is initially quite dark, with a lighter region emerging at the top of the coating. With the onset of fluid flow, the high-density region thins slightly but remains distinct. Looking more closely, the curve for t = 1.5 min in the corresponding Figure S30 shows three interfaces, separating (1) the coating and air, (2) the light and dark low-density layers, and (3) the low-density and high-density regions. Then from the curve corresponding to 3 min, we see that the dark low-density layer and the high-density region have become indistinguishable; the interface that previously existed gives way to a gentle gradient. Subsequent curves show only two interfaces (air/coating and light/dark) and the coating remains stratified into a lighter upper layer and a darker lower layer; it seems reasonable to now refer to the darker lower layer as the high-density region, as at longer times, it appears to correspond to the material that has deposited on the current collector. As we have noted earlier, we have classified "low-density" and "high-density" regions by their initial appearance alone, having lacked knowledge about how these evolve. We now recognize that despite initially distinct appearances, these regions do not necessarily remain distinct. At 12 min, we see a low-density region and a high-density region that both gradually grow darker with depth (presumably due to settling), then at 14 min, we see a lighter low-density region that has apparently lost material to the growing high-density region, which darkens more rapidly with depth. This trend continues at 15 min, at which we see an even lighter, nearly uniform low-density region and a rapidly darkening high-density region that has grown still thicker. Finally, at 16.5 min, we see a very stark transition from air to a very rapidly darkening high-density region, which we believe has consolidated into a nearly dry coating.

In the pixel value profiles for the 150 W experiment (Figure S31), the profile at 3 min suggests three interfaces, indicating that the darker layer in the low-density region is distinct from the high-density region (see the condensed time progression in Figure 6 for comparison). However, by 4 min, the interface between the dark low-density region and the high-density region has disappeared in favor of a gentle gradient, erasing the distinction between the darker low-density layer and the high-density region. Also as before, it seems reasonable to refer to this merged region as the high-density region, as at later times, it appears to make up the dense coating deposited on the current collector.

For this set of experiments, we have also plotted pixel values extracted from the condensed time-progression images of the standard deviations divided by means in Figures S32−S35. The largest variations occur where we expect phase contrast artifacts, near coating/substrate and air/coating interfaces, and at interfaces between coating layers (particularly in the plots corresponding to the 100 W experiment), which suggests some unevenness in interface heights above the substrate. High above the air/coating interfaces, the amount of variation is small; we consider this to be noise. In general, within the coating regions (or individual layers), variation along lines parallel to the coating/substrate interfaces appears to be small, as one should expect in coatings that should have good uniformity in the horizontal direction. More surprisingly, there appears to be a qualitative difference in the curves at earlier times and at later times, with a shift in average value, in all experiments. We suspect that there is a change in internal structure in the coatings, perhaps a change in particle agglomeration, that changes the uniformity of X-ray transmission. This tends to be observable a few minutes after the start of each experiment. However, these time intervals were shorter than those between the end of each mixing process and the start of the corresponding radiography experiment, which might indicate that some agglomeration occurred in all cases during sample transport, then was at least partially disrupted by the casting process, and that when left undisturbed, particles in the coatings agglomerated once again.

Having examined the images collected in experiments involving medium-concentration mixtures with unmodified PAA binder, we now turn our attention to the other mixture formulations described above.

3.2. Low-Concentration Silica/AB/Unmodified PAA/Water/IPA Samples. The condensed time-progression images are shown in Figures S3−S6, with the corresponding plots of transmission profiles at selected times shown for the lower heating powers in Figures S36−S38. In general, we expect these less-concentrated samples to flow easily. As with the medium-concentration samples, all of these show early increases in apparent coating height, which we earlier ascribed to fluid flow. As noted earlier, all of these dried coatings delaminated from the substrates when handled, presumably because there was insufficient binder attachment to the substrate, even when higher heating powers were applied. Due to this delamination, we did not obtain laminate thickness measurements. While binder concentrations relative to that of other dissolved or suspended components might be expected to determine local associations of material and might seem like a reasonable predictor for sufficiency of adhesion, we note that this was not the case: mass ratios among these components were the same as in the earlier "medium-concentration" experiments, and in the "high-concentration" experiments presented next.

Figure S3 (0 W) initially shows a coating with a high-density region that continuously decreases in apparent height over about 5 min, despite an increase in the thickness of the low-density region due to fluid flow during the same period. As in the experiments discussed earlier, we believe that this decrease primarily results from increasing platform tilt. This figure also shows two neighboring peaks in apparent height. The valley appears to coincide with the high-density region reaching a stable height, which we associate with the platform tilt reaching its limit. Based on this interpretation, the second peak occurs in the absence of continued platform tilt. At around the same time, we see decreasing transmission throughout the low-density region, hinting at material replacement in the field of view due to fluid flow. Following the second peak, we do not see abrupt changes in slope, in contrast with the medium-concentration images; perhaps fluid flow in this low-concentration coating subsides more gradually than in the medium-concentration experiments. Despite the low-density region showing relatively low transmission, it remains distinct from the high-density region until nearly the end of the observation. A faint outline of this interface is visible in the lower image of standard deviations divided by means and by the consistent behavior of corresponding pixel value curves near z = 0 at different times (Figure S36).

Figure S4 (50 W) initially shows a coating that consists of an unstratified low-density region and a high-density region. The coating then grows in apparent height, primarily due to an increase in apparent height of the high-density region. Unlike in the medium-concentration experiments (see, for example,

https://doi.org/10.1021/acsaem.4c00402
ACS Appl. Energy Mater. 2024, 7, 2989−3008

Figure S30), there are no abrupt pixel value transitions within the coating in corresponding transmission profile plots (Figure S37). This leads us to conclude that the dark region is a single high-density region rather than a dark low-density layer that has developed above a separate high-density region. This further suggests that the high-density region in this low-concentration mixture might be of fairly low viscosity and might move relatively freely. Fluid flow appears in this case to have primarily carried fairly concentrated fluid into the field of view. Starting at around 2.5 min, the low-density layer nearly vanishes for a few minutes. It then reappears for a few minutes (this is easier to see in the lower plot of relative error), whether due to material replacement by fluid flow or heat-driven separation, and then appears to concentrate and merge with the high-density region. In the transmission profile curves (Figure S37) at 7.5 and 10 min, the low-density layer is visible as a small region of steeper slope between two nearly horizontal regions corresponding to interfaces. From 7.5 to 10 min, the high-density region thins and becomes darker in the vicinity of the interface with the low-density region. From 10 to 15 min, there appears to be negligible change to the high-density region below the height of the interface at 10 min (that is, contribution of suspended material from the low-density region seems not to have had a significant effect on the transmission of the high-density region), and the high-density region comes to form the entirety of the dry coating.

Figure S5 (100 W) initially shows a coating consisting of a single high-density layer, which grows sharply but briefly. In the 50 W case (Figure S4), we attributed sharp growth in apparent thickness of the high-density region to fluid flow. However, in the present case, the high-density region soon decreases just as sharply in apparent height, so we instead suspect that the platform may have progressed from an initial counterclockwise tilt to a well-aligned state (see Figure S2), and then to a clockwise tilt. The high-density region then appears to stabilize in height, and a low-density layer appears, presumably due to fluid flow. We note that the increasing trend in the total apparent coating height is interrupted over the same interval, which reinforces our suspicion of platform tilt progression toward a limit. At around 1 min, a darker lower layer emerges in the low-density region. This is unlike stratification in the earlier medium-concentration experiments, in which a lighter layer emerged at the top of the low-density region under heating, so we suspect that this instead indicates material replacement in the field of view due to fluid flow. The dark lower layer grows in height as the upper layer thins, and then within another minute, this process appears to happen yet again. From the corresponding plots of mean transmission fraction curves in Figure S38, we see that by 3 min, there are no longer distinct low-density and high-density regions. Finally, at around 5.5 min, there is an abrupt relaxation in slope, and a mild change in slope at around 10 min. Following our interpretation of the medium-concentration results, we suspect that the latter corresponds to the end of appreciable flow, and the former corresponds to some obstruction of fluid flow. Finally, obvious delamination occurred just after the time interval shown in the condensed time-progression image, unfortunately before a stable apparent coating height was attained. The presence of delamination suggests that the coating edges (which tend to dry most quickly) were almost fully dry at the end of the time interval shown.

Figure S6 (150 W) initially shows a thin high-density region that begins to grow into a thicker region of concentrated material as a low-density region emerges above it at around 1 min. The low-density region darkens and merges into the high-density region at around 2 min, and another low-density region then emerges. As in the 50 W experiment, at peak apparent coating height, the high-density region accounts for most of the coating thickness. The apparent coating height then decreases, primarily due to a decrease in the apparent thickness of the high-density region, which suggests that the high-density region is quite mobile under fluid flow in this case. There is an abrupt relaxation of slope of the apparent coating height at about 5.5 min, along with a corresponding but somewhat milder change in the apparent height of the high-density region. For previous experiments, we inferred that similar changes in apparent coating height slope indicated some obstruction of fluid flow. Following this, at around 7 min, the apparent height of the high-density region has stabilized, which in previous experiments we might have associated with the end of fluid flow, but there is an abrupt change in slope of the apparent coating height, which surprisingly begins to increase. Based on the appearance of a later second peak in the earlier 100 W medium-concentration experiment, we suspect that this indicates substantial flow of the low-density region due to relaxation of excess fluid that was initially located far from the field of view. However, as in the 100 W low-concentration experiment, delamination clearly occurred shortly after the time interval shown, which suggests that the coating was nearly dry at the end of the interval. Finally, between about 10.5 and 13 min, the fluid flow must have come to an end and solvent must have been almost fully removed, yielding a nearly stable apparent coating height.

3.3. High-Concentration Silica/AB/Unmodified PAA/Water/IPA Samples. Condensed time-progression images for these experiments are shown in Figures S7−S10. All of the resulting dried coatings adhered sufficiently to the current collector to allow for handling without delamination, presumably because there was a sufficient attachment of binder to the substrate. Laminate thickness measurements are provided in Table S2. Unlike with the medium-concentration mixtures, the trailing edge heights are about equal or greater than those of the leading edges, and the center heights are closer to the edge heights. This suggests that these more concentrated coatings flowed in a somewhat different way than did the medium-concentration mixtures, perhaps with the fluid being moved more effectively by the passing doctor blade.

Figure S7 (0 W) shows a coating that is initially at its peak apparent height, in contrast to all of the other coatings that we have examined. This coating appears to consist of a low-density region with a single layer that is quite uniform in transmission and which decreases in height over time, with a change in slope of apparent height at around 1 min, which might coincide with the end of appreciable fluid flow. The higher mixture concentration might be impeding fluid flow and resisting stratification. The high-density region remains quite uniform in apparent height at earlier times, which suggests that the platform was fully tilted prior to $t = 0$. This region grows slightly in thickness as the low-density region decreases in thickness, which we expect as material deposits during the drying process.

The condensed time-progression images for experiments with higher heating powers (Figures S8−S10) show coatings that initially consist almost entirely of high-density regions and remain that way. Although this behavior is clearly distinct from the 0 W case, the coatings differ from the 0 W experiment from the outset, when the influence of heating is small as the lamp is still warming up. Therefore, we take these differences not as an indication of the influence of heating, but as an indication that

https://doi.org/10.1021/acsaem.4c00402
ACS Appl. Energy Mater. 2024, 7, 2989−3008

our casting process with manual sample deposition is not very reproducible. Figure S8 (50 W) shows an initial decrease in height, which we ascribe to progressing platform tilt, followed by the emergence of a persistent low-transmission top layer. Its persistence suggests that it is not a fluid region. We suspect that this reflects some nonuniformity in coating height along the beam direction, perhaps due to uneven drying or very subtle delamination. The large relative error at this interface in the bottom plot is consistent with nonuniformity. The 100 and 150 W images show almost no changes, suggesting that the platform was nearly fully tilted at the start of each experiment and that there was negligible fluid flow. For completeness, we have included these images as Figures S9 and S10. We suspect that there is negligible fluid flow in these experiments due to the relatively high mixture concentration and higher heating powers. Additionally, these mixtures may be less likely to escape under the doctor blade during casting than less concentrated mixtures and so would be spread more effectively, leading to coatings with more uniform initial thicknesses. However, coating height irregularities that do exist might be less able to relax before drying. Finally, the very modest changes in apparent coating height during drying suggest that the coatings are so concentrated that they might be understood as solvent-filled porous matrices of particles and binder.

3.4. Medium-Concentration Silica/AB/Li-PAA/Water/IPA Samples. Sample-condensed time-progression images for the medium-concentration mixtures using lithium-substituted PAA are shown in Figures S11−S14. As usual, we expect that the most transmissive regions within the resulting coating images (ignoring phase-contrast artifacts) should have a relatively low concentration of silica particles. However, we expect that the presence of lithium atoms in place of hydrogen atoms will make the PAA chains less compact, which might in turn affect interactions with the substrate and material distribution within the coatings (by influencing viscosity and particle motion). Even if our coating fabrication process were perfectly reproducible, these influences would prevent straightforward comparison of particle distributions with those from earlier experiments using unmodified PAA.

As with the high-concentration mixtures with unmodified PAA discussed previously, the results for samples with lithium-substituted PAA show more limited fluid flow than in the medium-concentration mixtures with unmodified PAA, consistent with our expectation that less compact polymer chains would produce more viscous samples. Laminate thickness measurements, shown in Table S3, indicate that these coatings are quite flat, but with a tendency for leading edges to be slightly thicker than trailing edges as in the unmodified PAA mixtures of medium concentration (Table S1). Comparison suggests that this might indicate flow behavior that is intermediate between that of the medium-concentration and high-concentration (Table S2) mixtures examined earlier, with the fluid being driven by the passing doctor blade with moderate effectiveness. The drying processes appear to be relatively short, perhaps due in part to limited fluid flow bringing a lower total volume of material into the field-of-view. As with the high-concentration mixtures with unmodified PAA, we attribute the variation in initial coating appearance and early flow to the limited reproducibility of the casting processes. Additionally, the high-density regions show little change in apparent thickness at earlier times, indicating that platform tilt stopped prior to observation in all of these experiments. The 0 W experiment (Figure S11) initially showed a prominent air bubble in the field of view, so the platform was moved at around 25 s; this abrupt change is particularly visible in the lower plot of relative error. Following the platform movement, the images show that the high-density region remains nearly constant in apparent height, and that the low-density region rises to a relatively low apparent peak height before receding, all without apparent stratification or abrupt changes in slope, which is reminiscent of the 0 W experiment with high concentration and unmodified PAA. In the 50 W experiment, shown in Figure S12, the coating in the field of view was initially very thin, so the platform was moved three times (at around 1, 1.1, and 1.5 min) in search of a thicker region, but with limited success. The coating remained thin, and the thin low-density region did not show stratification. Even at higher heating powers, unlike with the corresponding medium-concentration samples with unmodified PAA, the use of Li-PAA appears to have prevented heat-driven stratification, presumably because increased viscosity slows particle movement. Figure S13 (100 W) shows a coating with substantial initial apparent height, which then increases to a peak and then decreases, with no abrupt changes in slope between the peak and the final plateau. Unlike in the corresponding experiment with unmodified PAA and medium concentration, the low-density layer again does not show stratification. Neither does the 150 W experiment (Figure S14), in which the sample was moved once (at around 1.4 min) to seek a location at which the coating was thicker.

All of the medium-concentration mixtures with Li-PAA adhered sufficiently to the current collector to allow for handling without delamination. Unlike with the medium-concentration mixtures with unmodified PAA, neither the occurrence of stratification nor heating were necessary for good adhesion. Note that since the mass ratios of components were the same for both sets of mixtures, the mixtures with Li-PAA contain slightly fewer polymer chains per unit mass of the other components, and yet no heating was required to provide good adhesion. This further suggests indicates that lithium substitution in the PAA, while intended to change electrochemical properties, also changes mixture and coating properties.

3.5. Medium-Concentration Silica/AB/Cs-PAA/Water/IPA Samples. Condensed time-progression images are shown in Figures S15−S18. We expect that the most transmissive regions within the resulting coating images (ignoring phase-contrast artifacts) should have a relatively low concentration of silica particles and, because the cesium is particularly absorbing of X-rays, potentially binder as well. As with lithium substitution, we expect that cesium atoms substituted for hydrogen atoms will make the PAA chains less compact, affecting viscosity, material distribution, and surface interactions. These samples show more limited fluid flow than in the samples with medium concentration and unmodified PAA. Laminate thickness measurements, shown in Table S4, suggest fairly flat coatings, with the exception of the 150 W experiment, which shows high leading and trailing edges and might represent particularly inconsistent manual sample deposition.

The image for the 0 W experiment (Figure S15) initially shows a coating with substantial apparent height that continues to increase and then peaks and recedes. The high-density region shows an initial decrease to a stable apparent height, which, as in previous experiments, we attribute to the end of platform tilt progression. There are subtle changes in the slope of total apparent coating height at around 5 min (which we associate with some sort of obstruction of fluid flow) and 14 min (which we suspect to be the end of flow). In addition, within the low-density region, there is a persistent layer with high transmission

https://doi.org/10.1021/acsaem.4c00402
ACS Appl. Energy Mater. 2024, 7, 2989−3008

(which should correspond to low total concentrations of silica and Cs-PAA) that is adjacent to the high-density region and makes up the entire low-density region by the end of the experiment. As noted below, we see a similar feature in the 150 W experiment with the same sample. As we have not observed a similar behavior in other sets of experiments, we suspect that these features are visible due to the cesium substitution; in particular, the Cs-PAA might be relatively concentrated in the less transmissive top layer. While we recognize that cesium substitution influences mixture behavior, we cannot rule out the possibility that unmodified PAA was also relatively concentrated near the air/coating interface in other experiments but was not observable with radiography; increased concentrations near the surfaces of films can be driven by evaporation.[23] Finally, this less transmissive layer shrinks but does not appear to grow significantly more concentrated over time, perhaps due to fluid flow replacing material within the field of view.

The 50 W experiment (Figure S16) initially shows only a high-density region that appears to recede as a dark low-density region appears at the onset of fluid flow, which might indicate that some material from the high-density region is being agitated into the low-density region (an unusually slow tilt progression coinciding with the start of fluid flow would be very coincidental). Readers might find that the interface between these regions is more visible in the lower plot of relative error. The low-density region soon appears to stratify, with a lighter layer emerging at the top. This is unlike the corresponding experiments with a medium-concentration mixture and with standard PAA binder, which displayed no stratification at lower heating powers. Based on our expectation that particles will move less freely in the present samples, along with the appearance of stratification shortly after the start of fluid flow, we suspect that the apparent stratification is due to fluid flow replacing material in the field of view. Likewise, we suspect that material replacement causes the concentrated lower layer to show two peaks in height, while the apparent coating height has a single peak. The coating increases in apparent height only modestly and the lighter layer of the low-density region disappears by about 3 min. No abrupt slope transitions are otherwise visible. The dark low-density region and the high-density region are visibly distinct at the end of image collection, so this observation might have been terminated prematurely.

The 100 W experiment (Figure S17) initially appears to show a high-density region below a dark low-density region, and the low-density region rapidly grows more transmissive, which we suspect to result from material replacement through fluid flow. The low-density region apparent thickness rises to a peak and then decreases until disappearing fully, without stratifying and without abrupt changes in slope of apparent coating height, both of which were observed in the corresponding experiment with medium concentration and unmodified PAA. At the same time, the high-density region increases very modestly in apparent thickness, which is consistent with deposition of material from the low-density region.

In the first few minutes of observation, the coating shown in Figure S18 (150 W) increases in overall apparent height due to fluid flow, with the high-density region decreasing slightly in thickness. This decrease might result from progression of platform tilt, but due to its very gradual nature, we instead suspect that the high-density region is losing some material to the low-density region due to fluid agitation. The low-density region increases in thickness and then appears to stratify after about 15 s, with the emergence of a more transmissive lower layer that is reminiscent of that in the 0 W experiment in the present set of experiments. A more concentrated layer then emerges below the more transmissive layer at around 30 s. This behavior is distinct from the stratification observed in previous sets of experiments, in which lighter layers emerged above darker layers under sufficiently high heating power. Here, the emergence of the darker layer has not appeared to make the neighboring regions thinner or more transmissive, and at least initially, the increase in total apparent coating height comes almost entirely from the increase in thickness of the darker layer, so we suspect that the darker layer primarily contains material that has been carried into the field of view by fluid flow. Similar to the 0 W case, we expect that the lightest layer is a region of low total Cs-PAA and silica concentration, and that the top layer in the low-density region is relatively concentrated in Cs-PAA. Unlike in the 0 W experiment, all of the layers in the low-density region appear to concentrate over time and become integrated into the high-density layer, which might indicate that there is less fluid flow at later times in the present experiment.

In all of these experiments involving Cs-PAA, regardless of heating or possible differences in binder distribution, the dried coatings with Cs-PAA adhered well to the foil current collectors, while the dried coatings with unmodified PAA examined earlier only adhered well at higher (100 and 150 W) heating powers. We expect that less compact polymer chains promote adhesion to the substrate, despite the lower number density of polymer chains in the Cs-PAA mixtures (due to the mixture component mass ratios were the same whether using unmodified PAA or Cs-PAA). Similar to the Li-PAA mixtures, we conclude that cesium substitution does not simply change image contrast in these observations, but rather is changing the nature of the samples themselves.

3.6. NMC/AB/PVDF/NMP Samples. As with the more viscous water/alcohol-based mixtures examined earlier, we suspect that these coatings are relatively uniform in initial height as a consequence of the doctor blade more effectively pushing the higher-viscosity samples as opposed to allowing them to escape underneath.

The low AB, medium-concentration experiment (Figure S19) shows little change in apparent coating height over time, which is reminiscent of most of the relatively concentrated samples examined earlier, and we likewise attribute the present behavior to relatively high sample viscosity. Figure S39 shows the corresponding mean pixel value profiles. These do not suggest stratification or significant changes in transmission within the coating during the drying process. We also see a similar behavior in the corresponding experiments with a high concentration (Figures S20 and S23). The corresponding laminate thicknesses, provided in Table S5, show that the low AB, medium-concentration coating is quite uniform in thickness, but this is not the case for the low AB, high-concentration coating, for which the height increases from the leading edge to the trailing edge (again consistent with our suspicion that the doctor blade moves the more viscous fluids more effectively). Given the high concentration, we suspect that this profile is similar to what was initially produced by the casting action. Our observations were limited to the field of view, and we do not expect much fluid flow, so it appears that producing uniform coatings with our doctor blade will become difficult when viscosity is sufficiently high.

The high AB, medium-concentration experiment (Figure S22) initially shows a coating containing relatively transmissive material. The apparent height of the coating within the field of view is nearly constant for about 5 min, then decreases, and

https://doi.org/10.1021/acsaem.4c00402
ACS Appl. Energy Mater. 2024, 7, 2989−3008

shows slight variation prior to reaching a final value. The corresponding mean pixel value profiles are shown in Figure S40. These confirm that the coating representing the initial plateau is relatively transmissive, at least farther from the substrate, so significant fluid flow and/or volume loss from solvent evaporation seem plausible. There are no significant changes in transmission within the coating after the large decrease in apparent height.

Examining the processed radiography images directly (samples are shown in Figure S41), one can see small features in a thin bright region at the top of the coating. We observed that these small features are persistent, and based on the sizes of these features, we believe that these are individual NMC particles. Although most particles should be obscured by the bulk of the highly absorbing coating, we suspect that slight unevenness in height across the coating has placed this small collection of particles slightly higher than the other particles in the path of the beam. Just below this bright region, there are also particles which are visible but which appear to be in line with the bulk of the coating. These particular particles may be visible due to X-ray refraction at the air/coating interface, with bent light passing through a very small amount of coating material before reaching the scintillator. Examining consecutive images, we found that the particles move toward the leading edge of the coating over the entire observation interval, although at a much slower rate toward the end of the experiment. This is in the opposite direction of the doctor blade motion, so we suspect that the fluid flow in these relatively viscous samples is not driven by momentum, but rather by relaxation of excess fluid. Figure 9

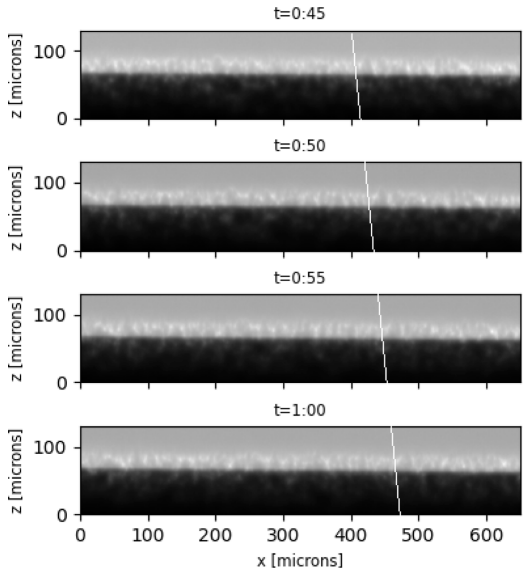

Figure 9. Sequence of profile images obtained for the NMC/PVDF/NMP mixture with low AB content and medium concentration (150 W heating power), shown close up with a line added to highlight horizontal motion of a visual feature.

shows consecutive profile images taken early in the observation, along with a line drawn to highlight the movement of a visual feature that moves through the field of view at approximately 4 μm/s; for this sample, total movements are therefore much smaller than the coating length (around 10 cm). Additionally, the sample was clearly dry by the end of the observation, so the very slight motion that we observed at longer times is surely not due to fluid flow; we believe that this is baseline movement of the entire apparatus due to settling or thermal expansion.

For additional context, the difference of the slopes of the air/coating interface and substrate is shown in the top plot in Figure S42. This is negative over most of the observation interval, which is consistent with the observed direction of fluid flow when the flow is driven by relaxation of excess fluid. However, despite the particles continuously moving toward the leading edge of the coating, the slope difference is positive during the interval over which the coating height decreases from its initial plateau to its long-term value. We speculate that simultaneous relaxation of multiple (and perhaps overlapping) fluid excesses in the vicinity of the field of view are driving flow toward the leading edge despite the local slope differences suggesting otherwise. We have provided an exaggerated illustration of a possible scenario in Figure S43, for which simultaneous relaxation of fluid excesses would drive fluid to the right, in the vicinity of the red observation box, due to the dominance of the largest excess, even if the slope visible in the box would suggest local flow to the left.

Figure S21 shows the condensed time progression for an NMP-based mixture with low AB content and low concentration. Radiography images showed large, persistent, relatively transmissive mounds with visible particles that clearly correspond to isolated irregularities in the field of view (see sample profiles in Figure S44). Although these features are undesirable in coating products and prevent our image analysis procedure from performing meaningful automatic detection of the air/coating interface, they fortuitously provide new information about these coatings. Stepping through the image sequence, we observed these mounds relaxing, with particles on either side of the peaks flowing in the "downhill" directions, as we expect. The mounds darken but do not relax fully before becoming static, at which point we presume that they are fully dried. This is direct evidence that fluid flow in these coatings can be driven by relaxation, that the direction of flow can change over a short distance due to nonuniform coating height, and that the competition between evaporation rate and fluid flow can influence final coating uniformity. The rest of the visible coating is dense and uniform, so no particles are visible.

Figure S24 shows the condensed time progression an NMP-based mixture with high AB content and low concentration. The platform was moved once during the experiment (slightly after 7.5 min), but despite this flaw, it is clear that there are changes in apparent height, presumably due to flow of more transmissive material, for this less viscous sample. Again stepping through the image sequence, we observed the visible particles flowing again from left to right (not shown here, but as in the earlier high AB, medium-concentration experiment). Like in the earlier experiment, movement is visible for the duration of the observation, although it is slow toward the end of the observation, which again must indicate only baseline movement of the apparatus itself when the coating is dry. The difference of the slopes of the air interface and substrate is shown in the bottom plot in Figure S42 and is negative over almost the entire observation, as we expect for the direction of fluid flow driven by relaxation of excess fluid. However, measurements of the dry coating thickness (Table S5) again indicate that the leading edge is slightly thicker than the trailing edge. As with the earlier high AB, medium-concentration results, we suspect that coating nonuniformities closer to the field of view have had a more significant influence on the direction of flow than does the material at the leading and trailing edges.

https://doi.org/10.1021/acsaem.4c00402
ACS Appl. Energy Mater. 2024, 7, 2989−3008

4. CONCLUSIONS

By constructing an automated coating and drying apparatus and using it in conjunction with the ALS hard X-ray microtomography/microradiography beamline, we have monitored the dynamic drying processes of composite electrode coatings. The apparatus is fundamentally a motorized platform, the coatings were cast using a doctor blade, as in typical laboratory-scale electrode fabrication, and drying was performed with an IR heating element in a manner intended to be of industrial relevance. We examined several battery electrode mixture samples and heated these under different IR power levels. Remote operation of the apparatus allowed us to capture radiography images of coatings starting within half a minute of casting. We developed an automated image analysis procedure for automatically and consistently processing the radiography images. We unfortunately detected platform tilt in each experiment, which limited quantitative image interpretation, although experimental evidence suggests that tilt progression stopped before or early in each observation. Despite the automated nature of our setup, reproducibility was limited because our experiments involved manual deposition of samples prior to casting. These issues will be addressed through improvements to the apparatus in future work. Despite these limitations, we observed several unexpected phenomena that have not been documented in the literature on composite electrode fabrication, to our knowledge.

We examined coatings produced from different formulations of silica, acetylene black (AB), water, isopropyl alcohol, and poly(acrylic acid) (PAA) and heated at different power levels. For many samples, we observed dramatic increases in apparent coating height, minutes after casting with the doctor blade. Analysis of our data, including micrometer measurements of the dry laminates following the radiography experiments, suggested that these temporary increases in coating height resulted from fluid flow within the coatings, parallel to the casting direction, with influences from momentum and gravity. We also demonstrated that coating edges did not move appreciably during the drying process, despite this internal flow. Also, as one might expect, higher-viscosity coatings showed less tendency to flow and to produce the large increases in apparent coating height.

We also documented different stages of behavior for these drying coatings, some of which involved continued fluid flow for several minutes or more after the casting process. All of these coatings showed higher-density regions above the substrates, presumably formed due to gravity-driven settling, existing from the start of observation (within about 30 s of casting) and typically showing little subsequent change. These regions typically accounted for most of the volume of the final dry electrode coatings. Above these higher-density regions were more mobile lower-density regions that could display heating-driven stratification. In some cases, heat-driven stratification was correlated with acceptable substrate adhesion of the dry electrode coatings. In other cases, mixture concentration appeared to determine whether sufficient substrate adhesion was attained.

We also performed similar experiments with mixtures using PAA with lithium or cesium substitutions. Such substitutions have been used by other researchers to alter electrode properties or to enable detection of the binder, but we expect that these changes affect polymer elongation, which might in turn influence distribution of material within the coatings. Coatings incorporating Li-PAA appeared to be more resistant to flow and did not show heat-driven stratification. Our coatings incorporating Cs-PAA behaved less consistently, but some of these coatings also showed higher resistance to flow, as well as subtle stratification into a surface layer with what we suspect to be a relatively high concentration of Cs-PAA, above a layer with a relatively low concentration of both Cs-PAA and silica; since unmodified PAA is very transmissive to hard X-rays, we are unable to observe if mixtures with unmodified PAA stratify in the same way. Based on these observations, we recommend using these modified binders cautiously, as these changes are likely to also alter mixture behavior and material arrangements in the dry electrodes, complicating comparison with electrodes made using unmodified PAA.

We also examined coatings produced from different formulations of lithium nickel manganese cobalt oxide (NMC) 622, polyvinylidene fluoride (PVDF), *n*-methyl-2-pyrrolidone (NMP), and AB. While these coatings were much more opaque to X-rays, we were fortuitously able to directly observe particle movement in thin surface layers, confirming the presence of fluid flow due to relaxation of excess fluid, even in these relatively viscous coating samples.

While these phenomena are surely highly dependent on the casting setup, we believe that they are potentially of general concern to all researchers producing electrode laminates using lab-scale techniques but which are intended for comparison with laminates produced using industrial-scale methods. To promote coating thickness uniformity when producing coatings with doctor blades (and likely, similar coating tools), one may want to limit fluid flow after casting, perhaps by preparing mixtures with sufficiently high viscosity or reducing casting speed to reduce fluid momentum. Based on our observations, we suspect that a higher viscosity can be helpful in ensuring that a mixture is spread effectively on a substrate and limiting fluid flow after casting. However, we have also observed that nonuniformities in coating height in casts of relatively viscous mixtures may not have sufficient time to relax before drying.

■ ASSOCIATED CONTENT

Supporting Information

The Supporting Information is available free of charge at https://pubs.acs.org/doi/10.1021/acsaem.4c00402.

Coating heights, substrate motion, sketches showing how alignment of platform and X-ray beam can limit coating visibility, condensed time-progression images, photographs showing stability of coating edges during drying, coating profile image sequences, plots of transmission and variation profiles, surface and substrate slope differences, and sketch and profile images of scenario showing overlapping excesses of fluid (PDF)

■ AUTHOR INFORMATION

Corresponding Author

Kenneth Higa − *Lawrence Berkeley National Laboratory, Berkeley, California 94720, United States;* orcid.org/0000-0003-4866-0748; Email: khiga@lbl.gov

Authors

Buyi Zhang − *Lawrence Berkeley National Laboratory, Berkeley, California 94720, United States; University of California, Berkeley, Berkeley, California 94720, United States*

https://doi.org/10.1021/acsaem.4c00402
ACS Appl. Energy Mater. 2024, 7, 2989−3008

Dilni Kaveendi Chandrasiri − *Lawrence Berkeley National Laboratory, Berkeley, California 94720, United States*
Denny Tan − *Lawrence Berkeley National Laboratory, Berkeley, California 94720, United States*
Daniel Collins-Wildman − *Lawrence Berkeley National Laboratory, Berkeley, California 94720, United States*
Patricius Bloemhard − *Lawrence Berkeley National Laboratory, Berkeley, California 94720, United States*
Eric Lizotte − *Lawrence Berkeley National Laboratory, Berkeley, California 94720, United States*
Gabriela Martin-Nyenhuis − *Lawrence Berkeley National Laboratory, Berkeley, California 94720, United States; RWTH Aachen University, Aachen 52056, Federal Republic of Germany*
Dilworth Y. Parkinson − *Lawrence Berkeley National Laboratory, Berkeley, California 94720, United States;* orcid.org/0000-0002-1817-0716
Ravi Prasher − *Lawrence Berkeley National Laboratory, Berkeley, California 94720, United States; University of California, Berkeley, Berkeley, California 94720, United States;* orcid.org/0000-0002-3282-7147
Vincent S. Battaglia − *Lawrence Berkeley National Laboratory, Berkeley, California 94720, United States*

Complete contact information is available at: https://pubs.acs.org/10.1021/acsaem.4c00402

Author Contributions

‖D.K.C., D.T., R.P. and V.S.B. contributed equally.

Notes

The authors declare no competing financial interest.

Disclaimer: This document was prepared as an account of work sponsored by the United States Government. While this document is believed to contain correct information, neither the United States Government nor any agency thereof, nor the Regents of the University of California, nor any of their employees, makes any warranty, express or implied, or assumes any legal responsibility for the accuracy, completeness, or usefulness of any information, apparatus, product, or process disclosed, or represents that its use would not infringe privately owned rights. Reference herein to any specific commercial product, process, or service by its trade name, trademark, manufacturer, or otherwise, does not necessarily constitute or imply its endorsement, recommendation, or favoring by the United States Government or any agency thereof, or the Regents of the University of California. The views and opinions of authors expressed herein do not necessarily state or reflect those of the United States Government or any agency thereof or the Regents of the University of California.

■ ACKNOWLEDGMENTS

We thank David Wood, Georgios Polyzos, Jaswinder Sharma, Kelsey Grady, AJ Kukay, and Erin Creel (now at Electric Hydrogen) of the Oak Ridge National Laboratory (ORNL) for their advice on pilot-scale coating processes and Scott Mauger and Mike Ulsh of the National Renewable Energy Laboratory (NREL) for their advice on mixture preparation. We thank Yanbao Fu and Adam Weber of Lawrence Berkeley National Laboratory (LBNL), Sarah Berlinger of LBNL and the University of California at Berkeley for their advice on lab-scale coating processes and mixture preparation, and Ohmar Sowle of LBNL for his advice in electronics construction. We also thank the ALS safety team for their support. This work was supported by the Assistant Secretary for Energy Efficiency and Renewable Energy, of the U.S. Department of Energy under contract no. DE-AC02-05CH11231, jointly through the Advanced Manufacturing Office, Vehicle Technologies Office, and Hydrogen and Fuel Cell Technologies Office. This research used resources of the Advanced Light Source, which is a DOE Office of Science User Facility under contract no. DE-AC02-05CH11231.

■ REFERENCES

(1) Hawley, W. B.; Li, J. *J. Energy Storage* **2019**, *25*, 100862.
(2) Zhang, Y. S.; Courtier, N. E.; Zhang, Z.; Liu, K.; Bailey, J. J.; Boyce, A. M.; Richardson, G.; Shearing, P. R.; Kendrick, E.; Brett, D. J. L. A Review of Lithium-Ion Battery Electrode Drying: Mechanisms and Metrology. *Adv. Energy Mater.* **2022**, *12*, 2102233.
(3) Morasch, R.; Landesfeind, J.; Suthar, B.; Gasteiger, H. A. Detection of Binder Gradients Using Impedance Spectroscopy and Their Influence on the Tortuosity of Li-Ion Battery Graphite Electrodes. *J. Electrochem. Soc.* **2018**, *165*, A3459−A3467.
(4) Pfaffmann, L.; Jaiser, S.; Müller, M.; Scharfer, P.; Schabel, W.; Bauer, W.; Scheiba, F.; Ehrenberg, H. New method for binder and carbon black detection at nanometer scale in carbon electrodes for lithium ion batteries. *J. Power Sources* **2017**, *363*, 460−469.
(5) Morelly, S. L.; Gelb, J.; Iacoviello, F.; Shearing, P. R.; Harris, S. J.; Alvarez, N. J.; Tang, M. H. Three-Dimensional Visualization of Conductive Domains in Battery Electrodes with Contrast-Enhancing Nanoparticles. *ACS Appl. Energy Mater.* **2018**, *1*, 4479−4484.
(6) Zhang, Y. S.; Bailey, J. J.; Sun, Y.; Boyce, A. M.; Dawson, W.; Reynolds, C. D.; Zhang, Z.; Lu, X.; Grant, P.; Kendrick, E.; Shearing, P. R.; Brett, D. J. L. Applications of advanced metrology for understanding the effects of drying temperature in the lithium-ion battery electrode manufacturing process. *J. Mater. Chem. A* **2022**, *10*, 10593−10603.
(7) Higa, K.; Zhao, H.; Parkinson, D. Y.; Barnard, H.; Ling, M.; Liu, G.; Srinivasan, V. Electrode Slurry Particle Density Mapping Using X-ray Radiography. *J. Electrochem. Soc.* **2017**, *164*, A380−A388.
(8) Fournier, R.; Shum, A. D.; Liu, J.; Sabarirajan, D. C.; Xiao, X.; Zenyuk, I. V. Combined Infrared Thermography, X-ray Radiography, and Computed Tomography for Ink Drying Studies. *ACS Appl. Energy Mater.* **2018**, *1*, 6101−6114.
(9) Yang, Y.; Xu, Z.; Steiner, J. D.; Liu, Y.; Lin, F.; Xiao, X. Quantitative probing of the fast particle motion during the solidification of battery electrodes. *Appl. Phys. Lett.* **2020**, *116*, 081904.
(10) Burdette-Trofimov, M. K.; Armstrong, B. L.; Nelson Weker, J.; Rogers, A. M.; Yang, G.; Self, E. C.; Armstrong, R. R.; Nanda, J.; Veith, G. M. Direct Measure of Electrode Spatial Heterogeneity: Influence of Processing Conditions on Anode Architecture and Performance. *ACS Appl. Mater. Interfaces* **2020**, *12*, 55954−55970.
(11) Hays, K. A.; Ruther, R. E.; Kukay, A. J.; Cao, P.; Saito, T.; Wood, D. L.; Li, J. *J. Power Sources* **2018**, *384*, 136−144.
(12) Sung, S. H.; Kim, D. H.; Kim, S.; Jeong, M. H.; Nam, J.; Ahn, K. H. Effect of neutralization of poly(acrylic acid) binder on the dispersion heterogeneity of Li-ion battery electrodes. *J. Mater. Sci.* **2019**, *54*, 13208−13220.
(13) Komini Babu, S.; Chung, H. T.; Zelenay, P.; Litster, S. Resolving Electrode Morphology's Impact on Platinum Group Metal-Free Cathode Performance Using Nano-CT of 3D Hierarchical Pore and Ionomer Distribution. *ACS Appl. Mater. Interfaces* **2016**, *8*, 32764−32777.
(14) Wu, C.-C.; Li, C.-C. Distribution Uniformity of Water-Based Binders in Si Anodes and the Distribution Effects on Cell Performance. *ACS Sustainable Chem. Eng.* **2020**, *8*, 6868−6876.
(15) Schneider, C.; Rasband, W.; Eliceiri, K. NIH Image to ImageJ: 25 years of image analysis. *Nat. Methods* **2012**, *9*, 671−675.
(16) Bradski, G. *Dr. Dobb's Journal of Software Tools*, 2000.
(17) Harris, C. R.; Millman, K. J.; van der Walt, S. J.; Gommers, R.; Virtanen, P.; Cournapeau, D.; Wieser, E.; Taylor, J.; Berg, S.; Smith, N. J.; et al. Array programming with NumPy. *Nature* **2020**, *585*, 357−362.

(18) Hunter, J. D. Matplotlib: A 2D Graphics Environment. *Comput. Sci. Eng.* **2007**, *9*, 90−95.
(19) *The ImageMagick Development Team ImageMagick*. https://imagemagick.org.
(20) Sutanthavibul, S.; Yap, K.; Smith, B. V.; King, P.; Sato, T.; Loimer, T. *Community Xfig 1985−2021*. http://mcj.sourceforge.net, 2021.
(21) Zhang, B.; Fan, B.; Huang, Z.; Higa, K.; Battaglia, V.; Prasher, R. A Review of Dispersion Film Drying Research. *J. Electrochem. Energy Convers. Storage* **2022**, *20*, 1−58.
(22) Førland, K. S.; Førland, T.; Ratkje, S. K. *Irreversible Thermodynamics: Theory and Applications*; John Wiley & Sons, 1988.
(23) Routh, A. F.; Zimmerman, W. B. Distribution of particles during solvent evaporation from films. *Chem. Eng. Sci.* **2004**, *59*, 2961−2968.

https://doi.org/10.1021/acsaem.4c00402
ACS Appl. Energy Mater. 2024, 7, 2989−3008